

# The Large Scale Structure of the Cosmic Microwave Background

E. B. Rørnes\*

*Institute of Physics, University of Oslo,  
0371 Oslo, Norway*

(Dated: May 28, 2024)

In this paper we present everything needed to create a Boltzmann-Einstein solver which calculates the CMB power spectrum in a simplified Lambda-Cold-Dark-Matter model. This is done by considering linear perturbations to the FLRW cosmology in the Newtonian gauge. First the completely flat background cosmology is computed where we later analyze recombination epoch. Finally we linearly perturb the background and compute the CMB and matter power spectrum. The formation of heavier atoms than hydrogen together with the effects of polarization and neutrinos are ignored throughout. This yields a rather significant discrepancy for small scale modes compared to more sophisticated methods, but is however accurate enough to understand the underlying mechanisms behind the CMB. The main results include: 1) various important epochs which are numerically calculated from the fiducial background cosmology, 2) the recombination history of the Universe, 3) how perturbations from initial conditions stemming from inflation allowed for overdensities to form large scale structures, and 4) a numerical approximation to the CMB and matter power-spectra.

## CONTENTS

Introduction	2	2.4. Summary	12
1. Background cosmology	2	3. Evolution of structure in the Universe	12
1.1. Theory	2	3.1. Theory	12
1.1.1. FLRW	2	3.1.1. Metric perturbations	12
1.1.2. $\Lambda$ CDM Model	3	3.1.2. Photon temperature fluctuations	13
1.1.3. Time and Distance Measurements in Cosmology	3	3.1.3. Matter density and velocity fluctuations	13
1.1.4. Markov-Chain Monte Carlo Method	4	3.1.4. Fourier transform and multipole expansions	14
1.2. Implementation details	4	3.1.5. Tight coupling	15
1.2.1. Solving the ODEs	4	3.1.6. Inflation	15
1.2.2. MCMC fit	5	3.1.7. Initial conditions	16
1.2.3. Python	5	3.2. Implementation details	17
1.3. Tests of data	5	3.3. Results	18
1.3.1. $\mathcal{H}'$ and $\mathcal{H}''$	5	3.3.1. Matter overdensity and bulk velocity	18
1.3.2. Conformal Time	6	3.3.2. Photon overdensity and bulk velocity	19
1.4. Results	6	3.3.3. Gravitational potentials	21
1.4.1. Time Evolution of Cosmic Parameters	6	3.4. Summary	22
1.4.2. Supernova Comparison	7	4. The CMB and matter power-spectra	22
1.5. Summary	8	4.1. Theory	23
2. Recombination history	8	4.1.1. Line-of-sight integration	23
2.1. Theory	9	4.1.2. CMB power spectrum	23
2.2. Implementation details	10	4.2. Implementation details	24
2.2.1. Solving the Saha and Peebles' equation	10	4.3. Results	24
2.2.2. Solving for the optical depth and visibility functions	11	4.3.1. Transfer function and integrand	24
2.3. Results	11	4.3.2. CMB power spectrum	25
2.3.1. Recombination Events	11	4.4. Matter power spectrum	26
2.3.2. Electron Fraction $X_e$	11	4.5. Summary	27
2.3.3. Evolution of Optical Depth and Visibility function	11	5. CMB map	27
		6. Conclusion	27
		Acknowledgments	27
		References	28

---

\* e.b.rornes@fys.uio.no

## INTRODUCTION

The cosmic microwave background (CMB) radiation is the oldest source of information that we currently have access to in our universe. This is then a vital piece of measurement which we can use to probe the evolution of the entire universe at very large scales. Today we observe that the temperature of the CMB photons coming from every direction is nearly the same with only minor fluctuations of order  $\sim 10^{-5}$  K. These photons, in a classical model, would have no possibility of causally interacting with one another to reach such an equilibrium. So the question is then; how did the photons coming from all directions in the sky become the same temperature? And why are there even any fluctuations at all? These are the main questions this paper will attempt to answer.

The overarching goal is to create a Boltzmann-Einstein solver which can numerically predict the CMB power spectrum and CMB map that we observe through observations. Along the way we will find many interesting results which require us to include both dark matter and dark energy as the current understanding of the evolution of the universe is not possible without these given current models. To do this we will first be starting off with the completely isotropic and homogeneous background cosmology in a so-called Lambda-Cold-Dark-Matter universe in section 1. In section 2 we will move over to probing the era of recombination. This is the time where neutral atoms begin to form as the energy density of the universe decays below a critical amount. Since the universe is neutral at this time, the photons decouple from the primordial plasma and are the CMB photons we see today. Next we will complicate our system by performing linear perturbations to the isotropic and homogeneous universe in section 3. Here we will use various Boltzmann equations and Einstein field equations to get our hands on various differential equations whose initial conditions will be set via an inflation model. Finally in section 4 we will be in a position to actually achieve our main goal of this project; to compute the CMB spectrum.

This project was built on the template provided by [1] which already contains a large part of the structure behind the numerical parts of the project. We will simplify the entire process by neglecting neutrinos, reionization and any heavier elements than Hydrogen. As we will see this has a noticeable effect on the numerical data, but is still a relatively good approximation. We will however still compute the effects of neutrinos in the background cosmology in section 1.

In the entire paper the subscript 0 denotes today's values whilst a superscript 0 represents an equilibrium. Note that throughout the article there are many switches between natural units where  $c = \hbar = k_b = 1$  and SI units.

## 1. BACKGROUND COSMOLOGY

In this section we consider the evolution of the uniform background of the universe in the Lambda-Cold-Dark-Matter ( $\Lambda$ CDM) model which is considered to be the present day standard model of cosmology. The main goal of this section is to solve the unperturbed background evolution of the universe by using known cosmological parameters supplied by [2] and comparing this to observational supernova data from [3].

### 1.1. Theory

#### 1.1.1. FLRW

In this milestone we approximate the universe to be completely isotropic and homogeneous over all scales. For large scales this has been shown to be a reasonable assumption from observations of the CMB power spectra [4]. The universe must then satisfy a maximally symmetric metric. With some symmetry arguments, we arrive at an exact solution for the metric called the Friedmann-Lemaître-Robertson-Walker (FLRW) metric. In flat space,  $k = 0$ , and Cartesian coordinates it is given by

$$g_{\mu\nu} = \text{diag} [-1, a^2(t), a^2(t), a^2(t)],$$

where  $a(t)$  is the scale factor, defined to be 1 today, and we are using the mostly plus metric signature  $(-, +, +, +)$ .

To make use of the line element above we consider the Einstein field equations (EFE):

$$G_{\mu\nu} + \Lambda g_{\mu\nu} = 8\pi G T_{\mu\nu}. \quad (1)$$

With the isotropy requirement, the stress-energy tensor which we will consider must be invariant under spatial rotations. The general stress-energy tensor is then on the form

$$T_{\mu\nu}(x) = \begin{bmatrix} T_{00}(x) & T_{0i}(x) \\ T_{0i}(x) & \sigma_{ij}(x) \end{bmatrix}.$$

As usual, the  $T_{00} = \rho$  component is to be interpreted as the energy density in a non-boosted frame. The requirement of homogeneity then imposes that one should not have any energy flux, as such  $T_{0i} = 0$ . The isotropy requirement imposes that the matrix  $\sigma$  must satisfy  $R^T \sigma(x) R = \sigma(x)$  for all  $x^\mu$  and rotation matrices  $R$ . The latter then implies that  $[R, \sigma(x)] = 0$ . As the generators of the  $SO(3)$  group form an algebra, Schurs' Lemma then states that this is satisfied iff  $\sigma(x) \propto I \implies \sigma_{ij}(x) = p(x)\delta_{ij}$  for some function  $p(x)$ . Furthermore the homogeneity requirement imposes translation invariance, meaning that  $p(x) = p(x + x_0)$ . With these requirements, a comoving observer, i.e. an observer in the rest frame of the universe, then implies

that we may uniquely describe the universe as a perfect liquid with

$$T_{\mu\nu} = (\rho + p)u_\mu u_\nu + g_{\mu\nu}p,$$

where  $p$  is to be interpreted as the pressure. As such, from the FRWL metric and the EFE one can derive the **Friedmann equations**:

$$\left(\frac{\dot{a}}{a}\right)^2 \equiv H^2 = \frac{8\pi G}{3}\rho, \quad (2)$$

$$\frac{\ddot{a}}{a} = -\frac{4\pi G}{3}(\rho + 3p). \quad (3)$$

### 1.1.2. $\Lambda$ CDM Model

The  $\Lambda$ CDM model is derived by assuming; that we have some family of weakly interacting massive particles (WIMPs) which we call cold-dark-matter (CDM) and a cosmological constant,  $\Lambda$ , which accounts for the present day acceleration of the universe, which will be the dark energy in this article. The name CDM comes from assuming that dark matter (DM) is massive enough to not be relativistic and hence cold. The first Friedmann equation (2) can be rewritten such that the time dependence of the **Hubble factor**  $H \equiv \dot{a}/a$  is given by

$$H^2 = H_0^2 \sum_i \Omega_{i0} a^{-3(1+\omega_i)}, \quad (4)$$

where  $\omega_i \equiv p_i/\rho_i$  is the equation of state for the  $i$ -th particle type,  $\Omega_i \equiv \rho_i/\rho_C$  is the relative energy density of the  $i$ -th particle type,  $\rho_i$  is the energy density corresponding to the  $i$ -th particle type and  $\sum_i \rho_i = \rho_C$  is the critical energy density required to have a flat universe which we observe today [2]. We have that  $\omega_B = 0$ ,  $\omega_R = 1/3$  and  $\omega_\Lambda = -1$  for baryons, relativistic particles (photons and massless neutrinos) and dark energy (DE) respectively. Simply plugging in the various particle types in (4) we have:

$$H = H_0 \sqrt{\Omega_{M0} a^{-3} + \Omega_{R0} a^{-4} + \Omega_{K0} a^{-2} + \Omega_{\Lambda0}}, \quad (5)$$

$$\Omega_{M0} \equiv \Omega_{B0} + \Omega_{CDM0}, \quad \Omega_{R0} \equiv \Omega_{\gamma0} + \Omega_{\nu0},$$

where  $\Omega_{B0}$ ,  $\Omega_{CDM0}$ ,  $\Omega_{\gamma0}$ ,  $\Omega_{\nu0}$  and  $\Omega_{\Lambda0}$  are then the present day relative densities of baryonic matter (electrons & protons), cold dark matter, radiation, neutrinos and dark energy respectively. The term  $\Omega_{K0} = -kc^2/H_0$  denotes the curvature of the universe and encapsulates how said curvature affects expansion rates and energy densities. With the requirement for a flat universe we have that  $\sum_i \Omega_i = 1$  where  $i$  refers to all non-curvature energy types. Since  $\Omega_B$ ,  $\Omega_{CDM}$  and  $\Omega_\gamma$ ,  $\Omega_\nu$  give the same contribution to the time evolution of the Hubble parameter, we will often bundle these together as “matter” and “radiation” (or “relativistic”) particles respectively as was done in (5).

The other Friedmann equation (3), together with each particles’ equation of state, is then used to describe how each quantity evolves with time:

$$\begin{aligned} \Omega_B(a) &= \frac{\Omega_{B0}}{a\mathcal{H}^2/H_0^2}, & \Omega_{CDM}(a) &= \frac{\Omega_{CDM0}}{a\mathcal{H}^2/H_0^2}, \\ \Omega_\gamma(a) &= \frac{\Omega_{\gamma0}}{a^2\mathcal{H}^2/H_0^2}, & \Omega_\nu(a) &= \frac{\Omega_{\nu0}}{a^2\mathcal{H}^2/H_0^2}, \\ \Omega_K(a) &= \frac{\Omega_{K0}}{\mathcal{H}^2/H_0^2}, & \Omega_\Lambda(a) &= \frac{\Omega_{\Lambda0}}{H^2/H_0^2}. \end{aligned} \quad (6)$$

Here  $\mathcal{H} \equiv aH$  is the **conformal Hubble factor**. Two of the six density parameters follow from the observed temperature of the CMB and are given by

$$\Omega_{\gamma0} = \frac{8\pi^3 G}{45H_0^2} \frac{(k_B T_{CMB0})^4}{\hbar^3 c^5}, \quad (7)$$

$$\Omega_{\nu0} = \Omega_{\gamma0} N_{\text{eff}} \cdot \frac{7}{8} \left(\frac{4}{11}\right)^{4/3}, \quad (8)$$

where  $T_{CMB0}$  is the temperature of CMB photons today and  $N_{\text{eff}} = 3.046$  is the effective number of massless neutrinos. [2]

The  $\Lambda$ CDM model is then fully determined by these cosmological observables which come from [2]

$$\begin{aligned} \frac{H_0 \text{ Mpc}}{100 \text{ km/s}} &\equiv h = 0.67, & N_{\text{eff}} &= 3.046, \\ \Omega_{B0} &= 0.05, & \Omega_{CDM0} &= 0.267, \\ \Omega_{K0} &= 0.00, & T_{CMB0} &= 2.7255. \end{aligned} \quad (9)$$

### 1.1.3. Time and Distance Measurements in Cosmology

Since the expansion of the universe is strictly positive w.r.t. time, the scale factor  $a(t)$  is an injective function and can thus be used as a time measurement. In this paper we will, for computational purposes, be using the variable  $x \equiv \ln(a) \implies a = e^x$ .

Again, due to the expansion of the universe, one can also measure how much the wavelength of a photon released at initial time  $t_i$  has stretched before it reaches us at final time  $t_f$ , commonly known as the **redshift**:

$$z = e^{x(t_f) - x(t_i)} - 1.$$

A derivation can be found in [5]. Since we are mainly interested in the redshift today where  $x(t_f) = 0$ , Thus the formula which will be used in this article is  $z = e^{-x(t_i)} - 1$ .

Further we consider the **horizon**, i.e. the “distance” massless particles may have travelled since the big bang. Since the universe is expanding due to  $\dot{a} > 0$ , this will be appreciably larger than  $ct$ . Considering a time  $t_1$ , light would have travelled a distance  $d_1 > ct_1$ . We can then consider what  $t_1$  must be such that this becomes an equality. For this we define the **conformal time**  $d\eta = dt/a$  (or conformal distance with the appropriate

insertion of  $c$ ) which can be rewritten as  $\eta(t) \equiv \int_0^t \frac{c}{a} dt'$ . Further rewriting this to a differential form we have

$$\frac{d\eta}{dx} = \frac{c}{\mathcal{H}}, \quad (10)$$

along with the initial condition  $\eta(-\infty) = 0$ , which can be solved analytically in the radiation dominated era. We will then use the analytical solution to approximate that at some very early time,  $x_{\text{start}}$  such that we have the new initial condition  $\eta(x_{\text{start}}) = c/\mathcal{H}(x_{\text{start}})$  where we will solve onwards numerically.

A useful distance measure is the **comoving distance**  $\chi$  which is derived by the FLRW metric:

$$\chi = \int_{t_i}^{t_0} dt \frac{c}{a} = \int_1^a da' \frac{c}{a'^2 H} = \int_0^z dz' \frac{c}{H} = \eta - \eta_0.$$

Considering a light-like path with the FLRW metric in curved space one can arrive at the **proper distance**  $r$ :

$$r = \begin{cases} \chi \frac{\sin(\sqrt{|\Omega_{K0}|} H_0 \chi / c)}{\sqrt{|\Omega_{K0}|} H_0 \chi / c}, & \Omega_{K0} < 0 \text{ "Closed"} \\ \chi, & \Omega_{K0} = 0 \text{ "Flat"} \\ \chi \frac{\sinh(\sqrt{|\Omega_{K0}|} H_0 \chi / c)}{\sqrt{|\Omega_{K0}|} H_0 \chi / c}, & \Omega_{K0} > 0 \text{ "Open"} \end{cases}.$$

We then consider the angular **diameter distance**  $d_A = \Delta s / \Delta \theta$  where  $\Delta s$  is the objects physical size and  $\Delta \theta$  its angular size as viewed from Earth. Once again from the FLRW metric, now in spherical coordinates:

$$ds^2 = -c^2 dt^2 + a^2(dr^2 + r^2 d\theta^2 + \sin^2 \theta d\phi^2),$$

one can find that this can be expressed in terms of our cosmological parameters as  $d_A = ar$ . The **luminosity distance**  $d_L$  is defined from  $d_L = \sqrt{\frac{L}{4\pi F}}$  where  $L$  is the intrinsic luminosity and  $F$  is the measured flux. As implied by its name, this quantity is related to  $d_A$  by  $d_L = d_A/a^2 = r/a$ .

At last we consider the **cosmic time**  $t$  in our  $x$  coordinate:

$$t(x) = \int_0^a \frac{da}{aH} = \int_{-\infty}^0 \frac{dx}{H(x)}.$$

From this we get to the ODE

$$\frac{dt}{dx} = \frac{1}{H}, \quad (11)$$

with the initial condition  $t(-\infty) = 0$ . This initial condition states that cosmic time begins once the big bang happened. As before, we make an analytical approximation which gives us the initial condition  $t(x_{\text{start}}) = \frac{1}{2H(x_{\text{start}})}$  and solved numerically from here.

#### 1.1.4. Markov-Chain Monte Carlo Method

In this milestone one of the major computational method which will be used is the Markov Chain Monte

Carlo (MCMC) method. The particular algorithm we use is the Metropolis algorithm which generates a Markov chain, where in each step, the chain corresponds to a proposed set of model parameters, which in our case are  $h, \Omega_{M0}$  and  $\Omega_{K0}$ . These parameters are sampled from a probability distribution guided by certain priors, i.e. accepted ranges, where data outside of these priors are omitted. The algorithm then eventually converges to the posterior distribution of the parameters given the observed data. This can then be used to constrain the cosmological parameters, in which we decide to focus on  $h, \Omega_{CDM0}$  and  $\Omega_{M0}$ . A  $\chi^2$ -test is then done by the assumption that the measurements are Gaussian distributed and uncorrelated between different redshift. The likelihood function is then given by  $L \propto e^{-\chi^2/2}$  where

$$\chi^2(h, \Omega_{M0}, \Omega_{K0}) = \sum_{i=1}^N [d_L(z_i, h, \Omega_{M0}, \Omega_{K0}) - d_L^{\text{obs}}]^2 / \sigma_i^2.$$

Here  $\sigma_i$  is the standard deviation for the  $i$ -th data point and  $N$  is the total number of data points. The set of parameters with the highest likelihood is our best-fit model, which also happen to be the values which minimize  $\chi^2$ . To check that this best-fit is in fact a good fit one can consider a set of data points which all lie exactly  $1\sigma$  away from the observed values. As such the sum simply reduces to  $N$ , implying that  $\chi^2/N = 1$ . Hence we will consider a best-fit to be a good fit if  $\chi^2 \sim N$ . For the case when  $\chi^2 \ll N$  then we over-fit the model, meaning we may be capturing random noise and fluctuations in the data, whilst if  $\chi^2 \gg N$  then we simply have a bad correspondence with the data and/or underlying assumptions (such as the assumption that the measurements are Gaussian).

## 1.2. Implementation details

### 1.2.1. Solving the ODEs

To implement some numerical tools to solve for the background we first implement the data from (9) and computed the derived quantities  $\Omega_{\gamma 0}$  and  $\Omega_{\nu 0}$  with (7, 8), and  $\Omega_{\Lambda 0} = 1 - \Omega_{\text{rest}0}$  where “rest” refers to all the other  $\Omega_i$ .

Next we implemented the Runge-Kutta 4 ordinary differential equation (ODE) solver to solve the ODEs for  $\eta(x)$  and  $t(x)$ . This was done by first setting up the respective differential equation (10, 11) with its corresponding initial condition. An ODE solver was used to get a result which was then splined. The ODE solver and splining programs were already provided in the template from [1].

Further we computed  $H(x)$  from (5) which was used together with the various relations from the theory section to compute  $\mathcal{H}, \frac{d\mathcal{H}}{dx}, \frac{d^2\mathcal{H}}{dx^2}, \Omega_i, r, d_A, d_L, \chi$  and  $T_{\text{CMB}}$  all as a function of our time variable  $x$ . Note that the expressions for  $\frac{d\mathcal{H}}{dx}$  and  $\frac{d^2\mathcal{H}}{dx^2}$  were found analytically from

(5). The calculated data was then written to data files to be analyzed in Python.

### 1.2.2. MCMC fit

We compared our numerical data for the luminosity distance  $d_L$  to observational data from [3], containing  $N = 31$  data points, by performing an MCMC fit. The upper and lower priors which were used are  $\{1.5, 1, 1\}$  and  $\{0.5, 0, -1\}$  for  $h, \Omega_M$  and  $\Omega_K$  respectively. The algorithm then computes an initial  $\chi^2$  with some randomly generated parameters. It repeats this process and checks whether the new  $\chi_{\text{new}}^2$  is less than the old  $\chi_{\text{old}}^2$ . If this is the case then it accepts this sample and starts again. However if this previous test is not the case we then perform a random check  $e^{-(\chi_{\text{new}}^2 - \chi_{\text{old}}^2)/2} > u$  where  $u$  is a number drawn from a uniform distribution in the interval  $[0, 1]$ . If it passes this test then  $\chi_{\text{new}}^2$  is accepted and the process carries on. This additional test is the main part of the Metropolis algorithm and is done to capture the full posterior probability distribution function (PDF) of the various parameters. As before, the data was printed to a data file and imported to Python.

### 1.2.3. Python

$x$ -values corresponding to radiation-matter and matter-DE equality were found by running a script over the data to find where the absolute value of the difference  $|\Omega_i - \Omega_j| = 0$ . In reality they were never quite 0 due to running over a discrete index, thus we simply set some low threshold, e.g.  $5 \cdot 10^{-5}$ . To find when the universe accelerates we note that

$$\mathcal{H} = \frac{\dot{a}}{a} \implies \frac{d\mathcal{H}}{dx} = \frac{d\mathcal{H}}{dt} \frac{dt}{dx} = \ddot{a} \frac{dt}{dx},$$

and from (11) we then have

$$\frac{d\mathcal{H}}{dx} \equiv \mathcal{H}' = \frac{\ddot{a}}{H}.$$

Since  $H$  is strictly positive we can then look at when  $\mathcal{H}'$  changes from negative to positive. So again a Python script which runs over the indices of  $\mathcal{H}'$  was used to find which  $x$ -value this sign change occurred, which corresponds to where the universe began to accelerate.

The MCMC-fit was then analyzed and a scatterplot in the  $\Omega_\Lambda \Omega_M$ -plane was created with the  $(1\sigma, 2\sigma)$  confidence regions  $\chi^2 - \chi_{\text{min}}^2 < (3.53, 8.02)$  respectively. These particular values were found from common  $\chi^2$  distribution tables with  $k = 3$  degrees of freedom. A histogram of the PDF from the accepted samples of  $h$  with a Gaussian fit along with a comparison of our theoretical  $d_L$  vs. the real supernova data were also plotted.

## 1.3. Tests of data

Before considering the results it is reasonable to conduct some sanity checks on the data to make sure everything was implemented correctly. To check that the data is consistent with the analytical expressions we consider the following quantities analytically in the different regimes:

$$\frac{\mathcal{H}'}{\mathcal{H}}, \quad \frac{1}{\mathcal{H}} \frac{d^2\mathcal{H}}{dx^2} \equiv \frac{\mathcal{H}''}{\mathcal{H}}, \quad \frac{1}{c} \eta \mathcal{H}.$$

### 1.3.1. $\mathcal{H}'$ and $\mathcal{H}''$

In the radiation dominated era where we approximate  $\Omega_R \approx 1 \implies \Omega_{\text{rest}} \approx 0$ . Then by using (5) we find

$$H_R(x) \approx H_0, \quad \mathcal{H}_R(x) \approx H_0 e^{-x},$$

$$\frac{\mathcal{H}'_R}{\mathcal{H}_R} \approx -1, \quad \frac{\mathcal{H}''_R}{\mathcal{H}_R} \approx 1,$$

and similarly using the approximations  $\Omega_M \approx 1$  and  $\Omega_\Lambda \approx 1$  respectively, we get

$$H_M(x) \approx H_0 e^{x/2}, \quad \mathcal{H}_M(x) \approx H_0 e^{-x/2},$$

$$\frac{\mathcal{H}'_M}{\mathcal{H}_M} \approx -1/2, \quad \frac{\mathcal{H}''_M}{\mathcal{H}_M} \approx 1/4,$$

$$H_\Lambda(x) \approx H_0, \quad \mathcal{H}_\Lambda(x) \approx H_0 e^x,$$

$$\frac{\mathcal{H}'_\Lambda}{\mathcal{H}_\Lambda} \approx \frac{\mathcal{H}''_\Lambda}{\mathcal{H}_\Lambda} \approx 1.$$

Plotting these assumptions with the data we have Fig. 1 we see that there is a reasonable agreement with the analytical approximations in the given regimes. As we will see in later,  $\Omega_M \approx 1$  is a relatively poor approximation compared to the others, hence larger a deviation is to be expected.

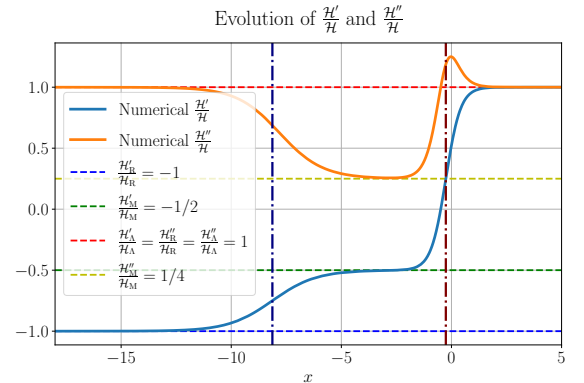


Fig. 1.  $\mathcal{H}'/\mathcal{H}$  and  $\mathcal{H}''/\mathcal{H}$  compared to analytical approximations in the various regimes where the left and right dash-dotted vertical lines signify radiation-matter equality and matter-dark energy equality respectively.

### 1.3.2. Conformal Time

Analytical approximations for the conformal time requires a little more effort. For the radiation dominated era we can solve (10) analytically:

$$\eta_R(x) = \int_{-\infty}^x \frac{c}{\mathcal{H}_R} dx' \approx \int_{-\infty}^x \frac{c}{H_0} e^{x'} dx' = \frac{c}{H_0} e^x.$$

Now we approximate this radiation dominated epoch to end abruptly at some time  $x_1$  such that we can write the conformal time in the matter dominated epoch as

$$\begin{aligned} \eta_M(x) &\approx \eta_R(x_1) + \int_{x_1}^x \frac{c}{\mathcal{H}_M} dx' \\ &\approx \frac{c}{H_0} \left( e^{x_1} + \int_{x_1}^x e^{x'/2} dx' \right) \\ &= \frac{c}{H_0} (e^{x_1} - 2e^{x_1/2} + 2e^{x/2}). \end{aligned}$$

Again we assume that the matter dominated epoch ends abruptly at some time  $x_2$  such that we can approximate

$$\begin{aligned} \eta_\Lambda(x) &\approx \eta_M(x_2) + \int_{x_2}^\infty \frac{c}{\mathcal{H}_\Lambda} dx' \\ &\approx \frac{c}{H_0} \left( e^{x_1} - 2e^{x_1/2} + 2e^{x_2/2} + \int_{x_2}^x e^{-x'} dx' \right) \\ &= \frac{c}{H_0} (e^{x_1} - 2e^{x_1/2} + 2e^{x_2/2} + e^{-x_2} - e^{-x}). \end{aligned}$$

Thus we find that for the various regimes we have the following:

$$\begin{aligned} \eta_R \mathcal{H}_R / c &\approx 1, \\ \eta_M \mathcal{H}_M / c &\approx (e^{x_1} - 2e^{x_1/2} + 2e^{x/2}) e^{-x/2}, \\ \eta_\Lambda \mathcal{H}_\Lambda / c &\approx (e^{x_1} - 2e^{x_1/2} + 2e^{x_2/2} + e^{-x_2} - e^{-x}) e^x. \end{aligned}$$

Using the  $x$  values corresponding to  $\Omega_R = \Omega_M$  and  $\Omega_M = \Omega_\Lambda$  as the time where the respective epochs start and end we get the graph in Fig. 2. Clearly this approximation will be nothing close to exact due to the assumption that the epochs end abruptly when in reality the epoch's change continuously and relatively slowly. Since  $\eta$  depends on how long the previous epochs lasted we can see that this heavily affects the final epoch.

Overall the data seems to be consistent with the analytical expressions, even if the conformal time is a rather difficult parameter to define a robust approximation for.

## 1.4. Results

Now that the data has been stress tested to show that they are at least valid in certain regions we can go on to look at some of the results.

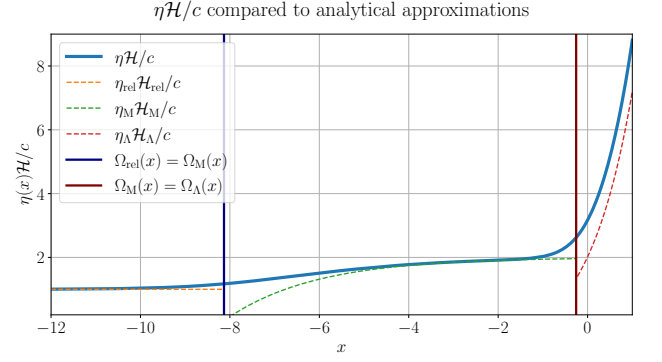


Fig. 2. Numerical  $\eta\mathcal{H}/c$  compared to analytical approximations in the various regimes where epochs are approximated to abruptly once  $\Omega_i = \Omega_j$ .

### 1.4.1. Time Evolution of Cosmic Parameters

We first consider the time evolution of the various relative energy densities  $\Omega_i$  as a function of the scale factor  $a(t)$  as given in Fig. 3.

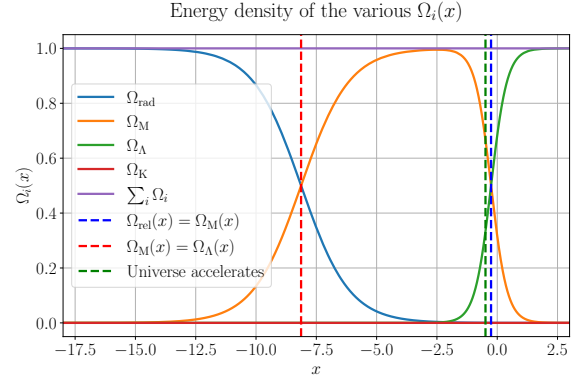


Fig. 3. Time evolution of the density parameters  $\Omega_i$  as a function of the scale factor  $a$ .

Here we can clearly see the different regimes of the various quantities. The early universe is in a complete radiation domination at early times which implies that the universe expands as  $a(t) \propto t^{1/2}$ . The universe then relatively slowly switches over to becoming matter dominated as time passes. For a short period of time we have complete matter domination, implying an expansion rate  $a(t) \propto t^{2/3}$ . Then dark energy starts to dominate at later times, causing the universe to begin to accelerate, until we get the known result of today where dark energy accounts for roughly 68% of the total energy in the universe today. It then further predicts that in the future, dark energy domination will continue to grow as time passes.

The time evolution of the conformal Hubble factor  $\mathcal{H}(x)$ , cosmic time  $t(x)$  and conformal distance  $\eta(x)/c$  is given in Fig. 4. The notable acceleration at later times in the  $\mathcal{H}$  plot can be seen by when the derivative of  $\mathcal{H}$

changes sign as mentioned previously. One can also see that this same phenomena affects both the cosmic time and conformal distance inversely at the same time. This is due to them both being inversely proportional to the conformal Hubble factor.

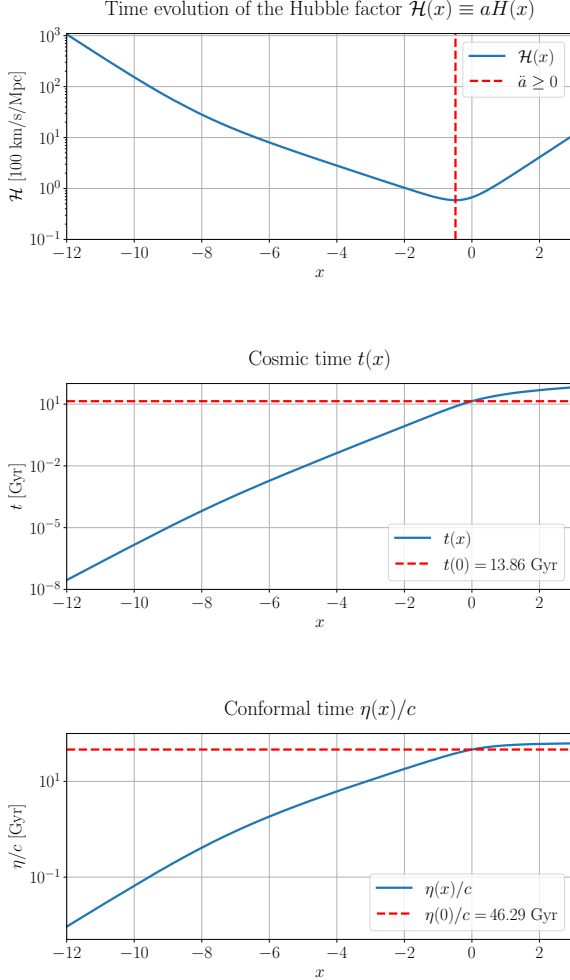


Fig. 4. Time evolution of the conformal Hubble factor  $\mathcal{H}$ , cosmic time  $t$  and conformal distance  $\eta/c$  as a function of  $x$ .

Next we consider the values of  $x, z, t, \eta, \Omega_M, \Omega_\Lambda$  and  $\Omega_R$  at various important events. A summary of these events is given in Table I.

Here we can see that radiation-matter-equality happened roughly 51000 years after the big bang. Further, the universe begins to accelerate roughly 7.7 billion years after the big bang. One may notice that this happens  $2\Omega_\Lambda \approx \Omega_M$  and  $\Omega_{\text{others}} \approx 0$ . At this time we have  $\Omega_{\text{tot}} \approx 3\Omega_\Lambda$  and hence  $\rho_{\text{tot}} = 3\rho_\Lambda$ . Further we have that  $p_{\text{tot}} = p_\Lambda + p_M = p_\Lambda$  due to  $p_M = 0$  from its equation of

state. Inserting this into the Friedman equation (3) with the relevant equation of state we get:

$$\begin{aligned} \frac{\ddot{a}}{a} &\approx -\frac{4\pi G}{3}(3\rho_\Lambda + 3(p_\Lambda + p_M)) \\ &= -\frac{4\pi G}{3}(3\rho_\Lambda - 3\rho_\Lambda) = 0 \end{aligned}$$

Now, since  $a$  is strictly a positive number then, mathematically, all that remains to check whether this is not when deceleration starts or a terrace point. To ensure this one can just check some arbitrarily close points such as  $\Omega_\Lambda = 1/3 \pm \epsilon$  and  $\Omega_M = 2/3 \mp \epsilon$  where  $\epsilon$  is some tiny positive number.

Next in the table we have  $t(x=0)$  which corresponds to the age of the universe today. [2] estimates this to be  $13.78 \pm 0.20$  Gly which is reasonably close to our value of 13.86 Gly. Similarly  $\eta(x=0)$  shows us the actual size of the observable universe today. [6] states the expected conformal distance of the universe is roughly 14 Gpc which corresponds to 45.7 Gly, again in reasonable agreement with the data.

#### 1.4.2. Supernova Comparison

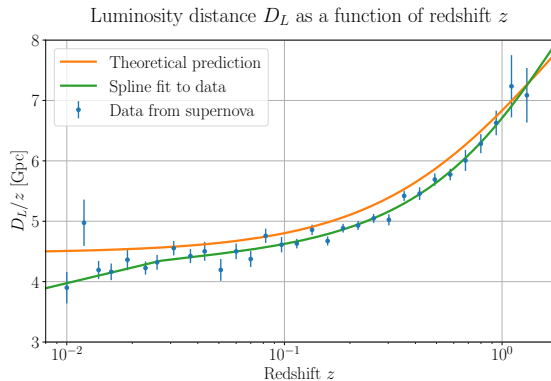
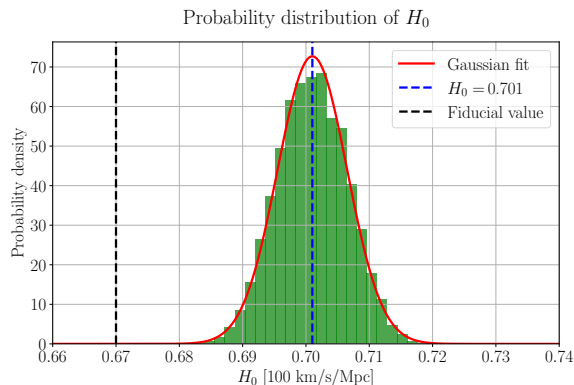
Further we compare our numerical data to data collected from supernova observations [3] by comparing the luminosity distance is given in Fig. 5 and making a posterior probability distribution function (PDF) of the Hubble parameter  $H_0$  in Fig. 6. We note that the found  $\chi^2_{\text{min}} = 29.3$  for the MCMC fit, which then yields that for the points accepted within the  $1\sigma$  region follow  $\chi^2 \sim N$  to a good approximation, suggesting that we have a good fit.

The luminosity distance from the observational data is seemingly always lower than our data. This phenomena is known as the **Hubble tension** which is a widely known problem in today's standard model of cosmology [7]. Direct data, such as supernova data, seemingly always prefers lower values for luminosity distance, and thus, higher values for  $h$  that can be seen in Fig. 6. Indirect data, such as the CMB, however prefer higher values for  $d_L$  and thus lower values  $h$  with much smaller errorbars. This is an ongoing issue which suggests that the  $\Lambda$ CDM model is not a complete model and must be modified. The posterior PDF of the Hubble parameter today  $H_0$  shows that the Gaussian fit is centered at roughly 70.1 km/s/Mpc. As mentioned, this is a large discrepancy from  $H_0 = 67$  km/s/Mpc which we got from the fiducial cosmology but still considered a common result from direct data.

Next we consider the scatterplot in the  $\Omega_\Lambda\Omega_M$ -plane shown in Fig. 7. The scatter-plot helps us visualize the degeneracy between the density parameters, i.e. that many different combinations of  $\Omega_M$  and  $\Omega_\Lambda$  can yield similar observational results. This leads to rather large degenerate regions in the parameter space. In this figure we can see that the flat universe constraint significantly

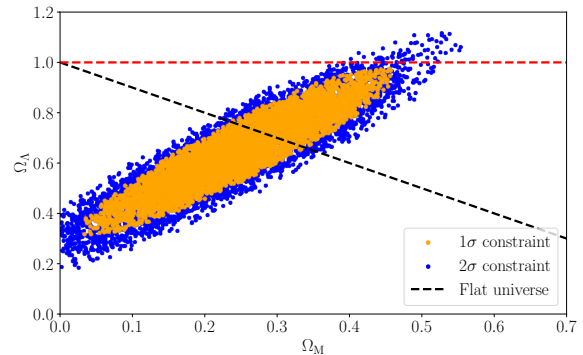
Table I. Results for cosmological parameters at various important events from numerical data.

Event	$x$	$z(x)$	$t(x)$ [Gly]	$\eta(x)/c$ [Gly]	$\Omega_M$	$\Omega_\Lambda$	$\Omega_{\text{Rel}}$
Radiation-Matter Equality	-8.132	3401	$5.106 \cdot 10^{-5}$	0.368	0.500	$2.737 \cdot 10^{-11}$	0.500
Universe Accelerates	-0.486	0.626	7.761	38.55	0.666	0.334	$3.183 \cdot 10^{-4}$
Matter-DE Equality	-0.256	0.292	10.38	42.33	0.500	0.500	$1.900 \cdot 10^{-4}$
Universe Today	0.000	0.000	13.86	46.29	0.317	0.683	$9.320 \cdot 10^{-5}$

Fig. 5. Luminosity distance over redshift  $z$ , plotted against redshift  $z$  for both; our numerical data, and observational data from Betoule et. al. [3] with error-bars.Fig. 6. Posterior PDF of the Hubble parameter  $H_0$  compared to the fiducial value  $H_0 = 67$  km/s/Mpc.

reduces this degeneracy by lowering the allowed parameters by orders of magnitude. The figure clearly shows that  $\Omega_{\Lambda 0} = 0$  is completely excluded given the observational data as this would be far outside the  $2\sigma$  constraint. The best-fit value for  $\Omega_{K0} = 0.067$  tells us that the universe is seemingly quite flat, but that there may indeed be some curvature. To test out whether this might just be an insensitivity to the  $\Omega_{K0}$  parameter the code was run again with a large initial value  $\Omega_{K0}$ . The result did not seem to change whatsoever and thus implies that our model is insensitive to the curvature of the universe.

Degeneracy between dark energy and matter density parameters in cosmology

Fig. 7. Supernova data with  $1\sigma$  and  $2\sigma$  constraints from MCMC fits.

### 1.5. Summary

We numerically solved the ODEs for  $\eta$  and  $t$  past the radiation domination. We then computed  $H(x)$  which gave us access to all the other relevant cosmological parameters. Further we checked that the numerical data corresponds to analytical approximations in the different regimes. Next we introduced all the most relevant data in a graphed form in Fig 4-6 such that important events and values were easily visualized. The most relevant values for the most important events in our background cosmology were summarized in Table I. Finally, an MCMC fit with observational data from supernova events and the numerical data in the  $\Omega_\Lambda$ - $\Omega_M$ -plane was made to consider some important aspects of our model, in particular that we cannot consider the current model without dark energy.

## 2. RECOMBINATION HISTORY

Next we look at the recombination history of the universe. This is when baryons, mainly protons and electrons, went from being ionized to forming neutral atoms once the energy of the photons dropped below 13.6 eV. As a result, photons during this time decoupled from the thermal equilibrium of the universe and are what we now detect as the CMB photons. As this event is tightly related to the free mean path of photons, the goal of this section is to compute the optical depth  $\tau$ , the visibility function  $\tilde{g}$  and their derivatives as these will be vital for



the next sections. In this section we only consider the formation of hydrogen and neglect the existence of any heavier atoms.

To accomplish this we start by calculating the free electron fraction  $X_e$  which we will first compute from the **Saha equation** in early times till  $X_e < 0.99$  and then switch over to the so-called **Peebles' equation** from thereon, both to be introduced in the theory section. The reason we don't use Peebles' equation from the start is due to it being extremely sensitive to high temperatures and thus the solution at early times is very unstable.

### 2.1. Theory

As eluded to in the intro we will consider the **optical depth**  $\tau(x)$  which is defined by the relation:

$$I(r) = I_0 e^{-\tau(r)}, \quad (12)$$

where  $I_0$  is the intensity of a source which emits radiation and  $I(r)$  is the intensity that an observer at a distance  $r$  would detect. Here we can clearly see that if  $\tau = 0$  then  $I(r) = I_0$  and thus the medium which the radiation travels through does not affect the intensity. If  $\tau \gg 1$  then we say that the medium is **optically thick**, if  $\tau \ll 1$  we say that the medium is **optically thin**, and  $\tau \sim 1$  is the transition between the two.

In cosmology the main effect contributing to the optical depth is Thompson scattering of photons with free electrons. The optical depth can be related to the Thompson scattering cross section via

$$\tau(\eta) = \int_{\eta}^{\eta_0} d\eta' n_e \sigma_T a, \quad (13)$$

$$\sigma_T = \frac{8\pi}{3} \frac{\alpha^2 \hbar^2}{m_e^2 c^2},$$

where  $n_e$  is the number density of free electrons. Note that since  $\sigma_T \propto m^{-2}$  we have neglected the scattering cross section of Thompson scattering with protons due to their relatively large mass. (13) can be rewritten into differential form:

$$\frac{d\tau}{dx} = -\frac{cn_e \sigma_T}{H}, \quad (14)$$

which is the ODE that we will solve. Since optical depth is 0 today we have the initial condition  $\tau(0) = 0$ . On the right hand side of (14), the only missing factor is  $n_e$ . Instead of computing  $n_e$  directly we will consider the fractional electron density:

$$X_e \equiv n_e/n_H \approx \frac{n_e m_H}{\rho_b} = \frac{n_e m_H a^3}{\Omega_{B0} \rho_{c0}},$$

where the approximation is due to us not considering any heavier elements than hydrogen. To do this we consider the Saha equation:

$$\frac{n_e n_p}{n_e^0 n_p^0} = \frac{n_H n_\gamma}{n_H^0 n_\gamma^0},$$

where  $n_p, n_\gamma$  and  $n_H$  are the number densities for free protons, photons and Hydrogen atoms respectively and the superscript 0 represents that the given number density is in thermal equilibrium. A derivation can be found in [4]. This is an analytical approximation for when the interaction rate is very high compared to the change in electron density. Since the early universe consists purely of free electrons due to the high temperatures of the primordial plasma, this then suggests that the Saha equation is only valid when  $X_e \approx 1$ . Given our definition of  $X_e$  and the approximations we can rewrite the Saha equation to the convenient form:

$$\frac{X_e^2}{1 - X_e} = \frac{1}{n_b} \left( \frac{k_b m_e T_b}{2\pi \hbar^2} \right)^{3/2} e^{-\epsilon_0/k_b T_b}, \quad (15)$$

where  $T_b$  is the baryon temperature of the universe and  $\epsilon_0 = 13.6$  eV is the ionization energy of hydrogen. In reality there should also be a  $T_\gamma$  in this equation representing the temperature of photons at a given time, but due to their tight coupling at early times, in practice it is an excellent approximation to set  $T_\gamma = T_b = T_{\text{CMB0}}/a$  [1]. The rewritten Saha equation is now simply a 2nd order polynomial in  $X_e$  which is easily solved analytically:

$$X_e = \frac{C}{2} \left[ \sqrt{1 + \frac{4}{C}} - 1 \right], \quad (16)$$

$$C \equiv \frac{1}{n_b} \left( \frac{k_b m_e T_b}{2\pi \hbar^2} \right)^{3/2} e^{-\epsilon_0/k_b T_b}, \quad (17)$$

where we have omitted the negative solution due to the electron fraction being manifestly positive. We also note that in the limit  $4/C \ll 1$  then  $X_e = 1$  which will be used in numerical calculations later.

Since the Saha equation is only valid for  $X_e \approx 1$  then, as noted earlier, we consider Peebles' equation outside this realm. The derivation for Peebles' equation is beyond the scope of this paper, but a simplified derivation can be found in [4] and is given by

$$\frac{dX_e}{dx} = \frac{C_r(T_b)}{H} \left[ \beta(T_b)(1 - X_e) - n_H X_e^2 \alpha^{(2)}(T_b) \right], \quad (18)$$

where

$$\begin{aligned}
C_r(T_b) &= \frac{\Lambda_{2s \rightarrow 1s} + \Lambda_\alpha}{\Lambda_{2s \rightarrow 1s} + \Lambda_\alpha + \beta^{(2)}(T_b)}, \\
\Lambda_{2s \rightarrow 1s} &= 8.227 \text{ s}^{-1}, \\
\Lambda_\alpha &= H \frac{(3\epsilon_0)^3}{(8\pi)^2 c^3 \hbar^3 n_{1s}}, \\
n_{1s} &= (1 - X_e) n_H, \\
n_H &= n_b, \text{ (no helium)} \\
n_b &= \frac{3H_0^2 \Omega_{b0}}{8\pi G m_H a^3}, \\
\beta^{(2)}(T_b) &= \beta(T_b) e^{\frac{3\epsilon_0}{4k_b T_b}}, \\
\beta(T_b) &= \alpha^{(2)}(T_b) \left( \frac{m_e k_b T_b}{2\pi \hbar^2} \right)^{3/2} e^{-\frac{\epsilon_0}{k_b T_b}}, \\
\alpha^{(2)}(T_b) &= \frac{8}{\sqrt{3\pi}} c \sigma_T \sqrt{\frac{\epsilon_0}{k_b T_b}} \phi_2(T_b), \\
\phi_2(T_b) &= 0.448 \ln \left( \frac{\epsilon_0}{k_b T_b} \right).
\end{aligned}$$

Note that here we take into account the  $2s$  energy level of the Hydrogen atom for more accurate data. This ODE will then be solved numerically to find  $X_e(x)$  with the initial condition given from the last  $X_e$  value from the Saha solution. This then gives us  $n_e(x)$  from the definition of  $X_e$  which will then be used to solve (14) for  $\tau(x)$ .

Further we define the visibility function as

$$\tilde{g}(x) \equiv \frac{d}{dx} e^{-\tau(x)} = -e^{-\tau(x)} \tau'(x). \quad (19)$$

This turns out to be a probability density function meaning that it satisfies

$$\int_{-\infty}^0 dx \tilde{g}(x) = 1.$$

The visibility function can be thought of as the probability that a photon scattering between time  $x$  and  $x+dx$  is the last time it ever scatters becoming a free streaming particle. From this we then define of **last scattering** as the time when the visibility function peaks. Once the solution to  $\tau(x)$  and its derivative have been established, getting the visibility function is a simple task.

Finally we have the sound horizon  $s(x)$  which is given by

$$s(x) \equiv \int_0^a dt \frac{c_s}{a}, \quad (20)$$

where  $c_s = c \sqrt{\frac{R}{3(1+R)}}$  is the sound-speed of the coupled photon-baryon plasma and  $R$  is given by

$$R = \frac{4\Omega_{\gamma 0}}{3a\Omega_{B0}}. \quad (21)$$

To interpret the sound horizon we consider an overdense region of the primordial plasma. This region will cause gravitational wells which will further cause a surplus of interactions between photons and baryons. These interactions cause an outwards pressure until the interactions begin to slow down again. The gravitational wells formed by dark matter then get deeper (as they do not feel this outward pressure), causing the same process to occur again. As such we expect oscillations of baryons and photons, which are comparable to propagating sound waves. The distance in which these sound waves may have travelled before recombination is what we define as the sound horizon. The reason why this quantity is particularly important is that once recombination occurs, the outward pressure will vanish. As such we expect to see overdensities begin to form on these rings after recombination.

We can rewrite (20) into a differential form as such:

$$\frac{ds}{dx} = \frac{c_s}{\mathcal{H}}. \quad (22)$$

Notice that in radiation domination we have that  $R \rightarrow \infty$ , implying that the sound speed  $c_s = c/\sqrt{3}$  giving us the initial condition

$$s(x_{\text{ini}}) = \frac{c_s(x_{\text{ini}})}{\mathcal{H}(x_{\text{ini}})} = \frac{c}{\sqrt{3}} \mathcal{H}^{-1}(x_{\text{ini}}).$$

## 2.2. Implementation details

### 2.2.1. Solving the Saha and Peebles' equation

We began by implementing a **for**-loop for the Saha equation which at each iteration checks whether we are still in the Saha regime. Note that we have to be careful about round-off errors when solving the Saha equation. When  $\epsilon_0/k_b T_b \rightarrow 0$  in the exponential in (17), the rest of the expression will begin to explode. Thus in (16) we would be subtracting two very large numbers, which should at the end simplify to just 1, leading to potential round-off errors. To avoid this we instead performed an **if**-test to check whether  $4/C$  is less than some small threshold. Once this is the case then we simply set  $X_e$  to 1, justified by considering the first order expansion of the square root in (16), which will just yield  $X_e = 1$ . Since the Saha equation is only valid for  $X_e \approx 1$ , we decide to switch over to the more accurate Peebles' equation once  $X_e < 0.99$ . For reference we continued on with the Saha equation past its validity to compare the results.

Peebles' equation was then solved numerically via the same ODE solver used in the previous milestone with the initial condition supplied by the last point before we exited the Saha regime. Some care was taken to ensure no overflow due to the exponential in the  $\beta^{(2)}$  equation under (18). To do this we simply created another **if**-test to check when the term in the exponential exceeded 150 and set  $\beta^{(2)} = 0$  as the exponential from  $\beta$  will dominate over it. We then had the results for  $X_e$  which we

used to compute  $n_e$  for both cases. The results for both the Saha only and the Saha-Peebles computations were splined and printed to a data file.

### 2.2.2. Solving for the optical depth and visibility functions

Next we solved the ODE for both the optical depth  $\tau(x)$  in (14) and the sound-horizon  $s(x)$  with the before mentioned initial conditions. Note that the prior ODE, if computed it in the usual way, would require subtracting an initial condition off the solution for  $\tau(x = 0)$ . Thus would lead to potential round-off errors close to  $x = 0$  due to the finite precision of floating point numbers, leading to noise in the solution. Thus the ODE was then instead solved by going backwards in time to avoid this problem. After,  $\tau'(x)$  was also computed since the spliner we are working with seemingly does not work well past 1st derivatives, as we also want an accurate spline of  $\tau''(x)$ . With both  $\tau(x)$  and  $\tau'(x)$  we could easily calculate the visibility function  $\tilde{g}(x)$  with (19) and its first derivative. These were then all splined along with using the `deriv_x` function in the spliner s.t. we have access to the 2nd derivatives. All the data was again printed to the aforementioned data file.

With the various splines we then calculated the time at recombination and last scattering. Our definition for when recombination happens is when  $X_e$  drops below 0.1 and the definition for when last scattering occurred is when  $\tilde{g}$  peaks. This was done by iterating through the data in C++ until these conditions were met.

As previously, the data was imported to Python and various plots together with a table of the various events were made.

## 2.3. Results

### 2.3.1. Recombination Events

We first consider the quantities  $x, z, y$  and  $r_s$  at both recombination and when last scattering occurred. The results are summarized in Table II. The times for recombination and last scattering both are in agreement previously found values [2]. [\[write more\]](#)

Table II. Recombination Events

Event	$x$	$z$	$t$ [kyr]	$r_s$ [Mpc]
Recombination	-6.9855	1079.8	377.96	145.278
Last scattering	-6.9853	1079.7	378.04	145.292

### 2.3.2. Electron Fraction $X_e$

The results for the electron fraction  $X_e$  are given in Fig. 8. Here we see that the moment the electron fraction

deviates even a small amount from  $X_e = 1$  then the Saha equation plummets, suggesting that recombination would happen at some time  $x \sim -7.14$  instead of the value given in Table II with Peebles' more accurate equation. In this figure, freeze out refers to the present day abundance of free electron which is estimated to be  $X_e(0) \approx 2.03 \cdot 10^{-4}$  with our numerical data.

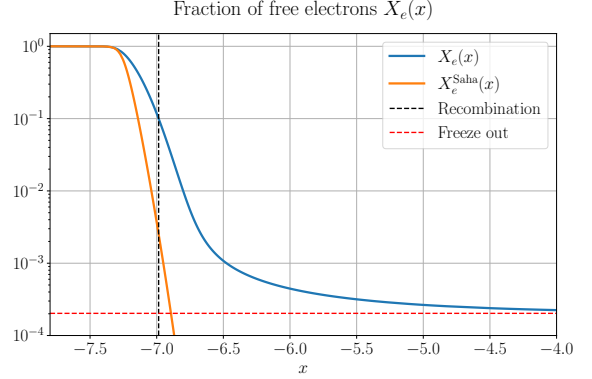


Fig. 8. Time evolution of the free electron fraction  $X_e(x)$ . Here the vertical line is the time of recombination and the horizontal line shows the present day abundance of free electrons.

### 2.3.3. Evolution of Optical Depth and Visibility function

Further we consider the time evolution of the optical depth parameter, the visibility function and their derivatives given in Fig. 9 and 10 respectively. The negative of the first derivative of  $\tau$  is plotted s.t. we can read off all of them in a single log-plot. For a similar reason the derivatives of  $\tilde{g}$  are normalized such that their peak is at  $\max \tilde{g}$ .

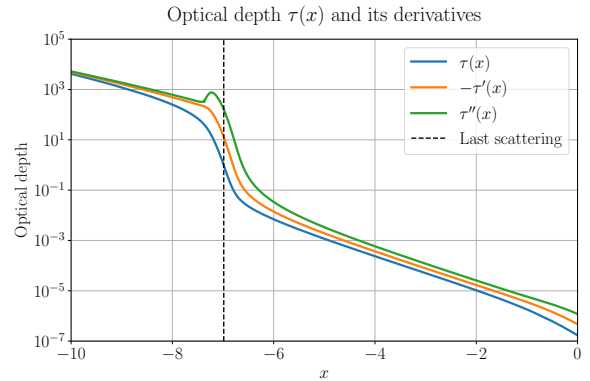


Fig. 9. Time evolution of the optical depth  $\tau(x)$  and its derivatives where the vertical line signifies the time of last scattering.

Before this dashed line signaling the last scattering event, the primordial plasma is optically thick. Thus the

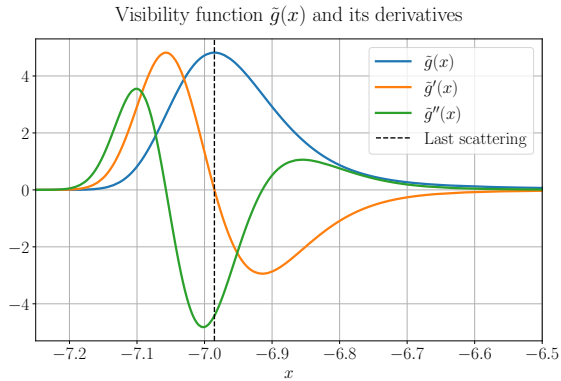


Fig. 10. Time evolution of visibility function  $\tilde{g}$  and its derivatives all normalized s.t.  $\max |\tilde{g}| = \max |\tilde{g}'| = \max |\tilde{g}''|$ . So that it all fits in the same plot. These factors are roughly 1/10 and 1/200 for  $\tilde{g}'$  and  $\tilde{g}''$  respectively.

mean free path of photons is too short and will continue scattering. However, the optical depth at this time still endures a stable decay almost solely due to the expansion rate of the universe as this causes the number density  $n_e$  to decrease as seen in (13). As mentioned previously, the visibility function is the probability density that a given photon had its last scattering at time  $x$ . Thus we can see that when the optical depth is very high, the likelihood of a particular photon at that time scattering for the last time is very small.

$\tau(x)$  then dips down violently as the number of free electrons in the universe rapidly decay. At the same time we then see that this is when the visibility function begins to rapidly increase. This clearly shows that the formation of neutral Hydrogen happens much faster than the expansion of the universe, hence having the largest effect in this epoch. This in turn means that the mean free paths of photons increase beyond their immediate vicinity; thus, photons are effectively free to travel without interacting with matter. This is when the last scattering event occurs and the photons released here are the ones that we detect today in the CMB spectra.

Once the electron fraction begins to flatten out again, the optical depth becomes a straight line on the log-plot, once again caused by the expansion of the universe. The visibility function also begins to flatten out at this point, albeit at a slower rate than the initial increase before last scattering, suggesting that some photons are not yet at their free streaming stage at these times.

## 2.4. Summary

We first solved the Saha equation due to Peebles' equation being stiff when the temperature of the universe was very high. We then switched over to use Peebles' equation once the fractional electron number density dropped sufficiently low. We then proposed times for when recombination and last scattering occurred within our model.

At last we had a discussion of the optical depth and the visibility function along with their physical relevance.

We can readily note from Fig. 10 that recombination and last scattering did not happen instantaneously, as  $\tilde{g}(x)$  would take the form of a Dirac-delta function, but instead over a relatively short period of time. Due to the short time frame, the number of free electrons in the universe rapidly decreased over several orders of magnitude. The values in Table II show us that recombination generally happens first, with the last scattering following shortly after.

As expected from the assumptions made in the derivation of the Saha equation, we see that it quickly becomes a terrible approximation outside of its regime. The manifestly seen correlation between the change in fraction of free electrons, optical depth and the visibility function is also clearly seen, but is of no surprise from their various relations.

## 3. EVOLUTION OF STRUCTURE IN THE UNIVERSE

The topic of this section is to see how small quantum fluctuations from the inflationary period caused small perturbations to the baryon, photon and dark matter fluid in the early which then grew into large structures formations we see today. Since we have determined various quantities of the background cosmology in the previous sections, all we need to do is to perturb the background and determine suitable initial conditions. To do this we write the perturbed flat FLRW metric in the Newtonian gauge. Note that from this section and onwards we set  $N_{\text{eff}} = 0$ , completely neglecting neutrinos from hereon.

### 3.1. Theory

#### 3.1.1. Metric perturbations

As mentioned in the intro we consider perturbations to the flat FLRW metric:

$$g_{\mu\nu} = g_{\mu\nu}^0 + h_{\mu\nu}, \quad |h_{\mu\nu}| \ll 1,$$

where  $g_{\mu\nu}^0$  is the pure FLRW metric and  $h_{\mu\nu}$  is a small perturbation. By  $|h_{\mu\nu}| \ll 1$  we mean that there exists some coordinate system where the components of  $h_{\mu\nu}$  satisfy this. The Newtonian gauge in Cartesian coordinates is defined by

$$h_{00} = -2\Psi, \quad h_{0i} = 0, \quad h_{ij} = 2a^2\delta_{ij}\Phi,$$

where  $\Psi = \Psi(t, \mathbf{x})$  and  $\Phi = \Phi(t, \mathbf{x})$  are scalar perturbations of the flat FLRW metric which happen to be the Newtonian potential and the Newtonian curvature respectively. Note that this implies  $\Psi \ll 1$  and  $\Phi \ll 1$ .

As such the line element in Cartesian coordinates and the Newtonian gauge takes the form

$$ds^2 = -(1 + 2\Psi)dt^2 + a^2(t)(1 + 2\Phi)d\mathbf{x}^2.$$

### 3.1.2. Photon temperature fluctuations

Since we are interested in solving perturbations to the Boltzmann equations for the various particle types we first consider the Boltzmann equation for photons:

$$\frac{df}{dt} = C[f],$$

where  $f = f(\mathbf{x}, \mathbf{p}, t)$  is the Bose-Einstein distribution due to photons being relativistic integer spin particles and  $C[f]$  is the collision term due to Thompson scattering. Expanding the total derivative on the left via the chain rule yields:

$$\frac{df}{dt} = \frac{\partial f}{\partial t} + \frac{\partial f}{\partial \mathbf{x}} \frac{d\mathbf{x}}{dt} + \frac{\partial f}{\partial |\mathbf{p}|} \frac{d|\mathbf{p}|}{dt} + \frac{\partial f}{\partial \hat{\mathbf{p}}} \frac{d\hat{\mathbf{p}}}{dt}, \quad (23)$$

where  $\hat{\mathbf{p}} = \mathbf{p}/|\mathbf{p}|$  is the direction of the photon propagation. Using the geodesic equation and the metric whilst only keeping first order terms, one can show that (23) can be rewritten to a more convenient form:

$$\frac{df}{dt} = \frac{\partial f}{\partial t} + \frac{p}{E} \frac{\hat{\mathbf{p}}}{a} \frac{\partial f}{\partial \mathbf{x}} - |\mathbf{p}| \frac{\partial f}{\partial |\mathbf{p}|} \left[ H + \frac{d\Phi}{dt} + \frac{E}{a} \frac{\hat{\mathbf{p}}}{|\mathbf{p}|} \frac{\partial \Psi}{\partial \mathbf{x}} \right]$$

Since we know the CMB is roughly  $T^0 = 2.7255 \text{ K}$  with small fluctuations around this average, we then define the perturbation about this equilibrium:

$$T(\mathbf{x}, \hat{\mathbf{p}}, t) = T^0[1 + \Theta(\mathbf{x}, \hat{\mathbf{p}}, t)].$$

One can show that all terms dependent on the magnitude of the momenta stemming from the Boltzmann equation for photons, can be rewritten in terms of  $\Psi$  and  $\Phi$  to first order. As such the collision term for Thompson scattering in the Boltzmann equation then takes the form

$$C[f(\mathbf{p})] = -p \frac{\partial f^0}{\partial p} n_e \sigma_T [\Theta_0 - \Theta(\hat{\mathbf{p}}) + \hat{\mathbf{p}} \cdot \mathbf{v}_b], \quad (24)$$

where  $\mathbf{v}_b$  is the bulk velocity of baryons. A more in-depth derivation can be found in [4]. As mentioned in the prior section, we can ignore the contributions from protons as  $m_p \gg m_e$  since the Thompson cross section  $\sigma_T \propto m^{-2}$ . Thus in practice it really only specifies the bulk velocity of electrons before recombination. The other side of the Boltzmann equation for photons to first order is:

$$\frac{df}{dt} = -p \frac{\partial f^0}{\partial p} \left[ \frac{\partial \Theta}{\partial t} + \frac{\hat{\mathbf{p}}}{a} \frac{\partial \Theta}{\partial \mathbf{x}} + \frac{d\Phi}{dt} + \frac{\hat{\mathbf{p}}}{a} \frac{\partial \Psi}{\partial \mathbf{x}} \right]. \quad (25)$$

Equating (24) and (25) yields the Boltzmann equation for radiation to first order:

$$\frac{\partial \Theta}{\partial t} + \frac{\hat{\mathbf{p}}}{a} \frac{\partial \Theta}{\partial \mathbf{x}} + \frac{d\Phi}{dt} + \frac{\hat{\mathbf{p}}}{a} \frac{\partial \Psi}{\partial \mathbf{x}} = n_e \sigma_T [\Theta_0 - \Theta(\hat{\mathbf{p}}) + \hat{\mathbf{p}} \cdot \mathbf{v}_b]. \quad (26)$$

Fourier transforming this and defining  $\mu \equiv \hat{\mathbf{p}} \cdot \mathbf{k}/|\mathbf{k}|$  where  $\mathbf{k}$  is the Fourier mode we can bring this into the form [1]

$$\begin{aligned} \frac{\partial \Theta}{\partial t} + \frac{ik\mu}{a} \Theta + \frac{\partial \Phi}{\partial t} + \frac{ik\mu}{a} \Psi \\ = n_e \sigma_T \left[ \Theta_0 - \Theta + i\mu v_b - \frac{P_2(\mu)}{2} \Theta_2 \right], \end{aligned} \quad (27)$$

where  $P_2$  is the second order Legendre polynomial. We will come back to this last equation in section 4.

### 3.1.3. Matter density and velocity fluctuations

Next we consider the Boltzmann equation for CDM. As mentioned in section 1 we consider CDM to be WIMPs, meaning their collision term is simply null. As mentioned earlier, CDM are non-relativistic particles, and thus their distribution function can be modelled as a Maxwell-Boltzmann distribution. Considering them to act as a perfect liquid and following a similar procedure one arrives at the cosmological generalization of the continuity equation and Euler equation respectively:

$$0 = \frac{\partial n}{\partial t} + \frac{1}{a} \frac{\partial(n\mathbf{v})}{\partial \mathbf{x}} + 3n \left[ H + \frac{\partial \Phi}{\partial t} \right], \quad (28)$$

$$0 = \frac{\partial \mathbf{v}}{\partial t} + H\mathbf{v} + \frac{1}{a} \frac{\partial \Psi}{\partial \mathbf{x}}. \quad (29)$$

Here we have suppressed the CDM label on the number density  $n \equiv n_{\text{CDM}}$  and the bulk velocity  $\mathbf{v} \equiv \mathbf{v}_{\text{CDM}}$  for readability. Further considering perturbations about the mean number density  $n^0$ :

$$n(\mathbf{x}, t) = n^0[1 + \delta(\mathbf{x}, t)].$$

The first order contribution to (28) is then

$$\frac{\partial \delta}{\partial t} + \frac{1}{a} \frac{\partial \mathbf{v}}{\partial \mathbf{x}} + 3 \frac{\partial \Phi}{\partial t} = 0. \quad (30)$$

Baryons are also considered to behave as a non-relativistic fluid, meaning they satisfy Maxwell-Boltzmann distributions. The main difference between baryons and CDM is that they can interact amongst themselves and photons, the latter being via Thompson scattering. As mentioned in section 2, Thompson scattering via protons can be neglected due to the cross section being inversely proportional to the square of the mass of the scattered particle. The perturbations to the cosmological continuity equation takes the same form as (30), i.e.

$$\frac{\partial \delta_B}{\partial t} + \frac{1}{a} \frac{\partial \mathbf{v}_B}{\partial \mathbf{x}} + 3 \frac{\partial \Phi}{\partial t} = 0. \quad (31)$$

However the corresponding Euler equation takes a different form due to interactions:

$$\frac{\partial \mathbf{v}_B}{\partial t} + H\mathbf{v}_B + \frac{1}{a} \frac{\partial \Psi}{\partial \mathbf{x}} = -n_e \sigma_T R(\mathbf{v}_\gamma - \mathbf{v}_B), \quad (32)$$

where  $R$  is defined in (21) and the parenthesis on the right hand side corresponds to the momentum transfer in the scattering process.

### 3.1.4. Fourier transform and multipole expansions

As of now all the relevant equations are all partial differential equations (PDEs) which remain tough to solve. Thus we wish to express these in terms of ODEs instead as this is something we know how to solve. We first consider the temperature perturbations  $\Theta$ . Since we are in general interested in the perturbations on various different scales in a mostly spherically symmetric universe we consider rewriting our functions in terms of multipole expansions. These are a series written in terms of Legendre polynomials  $P_l(\zeta \equiv \cos \theta)$ :

$$\Theta(t, k, \zeta) = \sum_{\ell=0}^{\infty} \frac{2\ell+1}{i^\ell} \Theta_\ell(t, k) P_\ell(\zeta).$$

The Legendre polynomials are orthonormal and form a complete basis. As such we can invert this equation in the same way as one would for Fourier coefficients to attain the Legendre multipoles:

$$\Theta_\ell(t, k) = \frac{i^\ell}{2} \int_{-1}^1 d\zeta \Theta(t, k, \zeta) P_\ell(\zeta).$$

The most relevant moments are: the monopole  $\Theta_0 = \frac{1}{4}\delta_\gamma$ , the dipole  $\Theta_1 = -\frac{1}{3}v_\gamma$  and the quadrupole  $\Theta_2$ . One can then recursively find all the Legendre polynomials by using Bonnet's recursion formula:

$$\zeta P_\ell = \frac{\ell+1}{2\ell+1} P_{\ell+1} + \frac{\ell}{2\ell+1} P_{\ell-1}.$$

Then, bringing (26) into Fourier space, switching to conformal time, using the above mentioned tricks together with the orthonormality of the Legendre polynomials, rewriting everything in terms of  $x$ , and reintroducing SI-units one find that the time dependence of the multipoles are given by:

$$\begin{aligned} \Theta'_0 &= -\frac{ck}{\mathcal{H}} \Theta_1 - \Phi', \\ \Theta'_1 &= \frac{ck}{3\mathcal{H}} \Theta_0 - \frac{2ck}{3\mathcal{H}} \Theta_2 + \frac{ck}{3\mathcal{H}} \Psi + \tau' \left[ \Theta_1 + \frac{v_B}{3} \right], \\ \Theta'_\ell &= \frac{\ell ck}{(2\ell+1)\mathcal{H}} \Theta_{\ell-1} - \frac{(\ell+1)ck}{(2\ell+1)\mathcal{H}} \Theta_{\ell+1}, \\ &\quad + \tau' \left[ \Theta_\ell - \frac{\Theta_\ell}{10} \delta_{\ell,2} \right], \quad \ell \geq 2, \end{aligned}$$

where the primes, as before, represent derivatives w.r.t.  $x = \ln(a)$ ,  $k$  is the corresponding Fourier coefficient and  $v$  is defined via the relation  $\mathbf{v} = i\mathbf{k}v$ .

Next we consider the scalar potentials  $\Phi$  and  $\Psi$  which can be found from the EFE. After some work one arrives at the following equations:

$$\begin{aligned} \Phi' &= \Psi - \frac{1}{3} \left( \frac{ck}{\mathcal{H}} \right)^2 \Phi + \frac{1}{2} [\delta\Omega_{\text{CDM}} + \delta_B\Omega_B + \delta_\gamma\Omega_\gamma], \\ \Psi &= -\Phi - 12 \left( \frac{\mathcal{H}}{ck} \right)^2 \Omega_\gamma \Theta_2. \end{aligned}$$

An in-depth derivation for this result can be seen in [4].

Further, to simplify the problem of solving number density perturbations  $\delta$  and bulk velocity  $v$  for baryons and CDM we begin by expressing them in terms of conformal time and further translate them over to Fourier space to arrive at:

$$\begin{aligned} \dot{\delta} &= -3\dot{\Phi} + kv, \\ \dot{v} &= -k\Psi - \mathcal{H}v, \\ \dot{\delta}_B &= -3\dot{\Phi} + kv_B, \\ \dot{v}_B &= -k\Psi + \dot{\tau}R(v_B - v_\gamma) - \mathcal{H}v_B. \end{aligned}$$

As before we switch over to our time variable  $x$  and use some of the relations between the multipoles. The results are summarized in equations (33, 34, 35) where  $\ell_{\text{max}}$  refers to the highest order multipole which we compute.

#### Photon temperature multipoles

$$\Theta'_0 = -\frac{ck}{\mathcal{H}} \Theta_1 - \Phi', \quad (33a)$$

$$\Theta'_1 = \frac{ck}{3\mathcal{H}} \Theta_0 - \frac{2ck}{3\mathcal{H}} \Theta_2 + \frac{ck}{3\mathcal{H}} \Psi + \tau' \left[ \Theta_1 + \frac{1}{3} v_B \right], \quad (33b)$$

$$\Theta'_2 = \frac{2ck}{5\mathcal{H}} \Theta_1 - \frac{3ck}{5\mathcal{H}} \Theta_3 + \frac{9}{10} \tau' \Theta_2, \quad (33c)$$

$$\Theta'_\ell = \frac{\ell ck}{(2\ell+1)\mathcal{H}} \Theta_{\ell-1} - \frac{(\ell+1)ck}{(2\ell+1)\mathcal{H}} \Theta_{\ell+1} + \tau' \Theta_\ell, \quad (33d)$$

Above is valid for  $2 < \ell < \ell_{\text{max}}$ ,

$$\Theta'_{\ell_{\text{max}}} = \frac{ck}{\mathcal{H}} \Theta_{\ell_{\text{max}}-1} - c \frac{\ell+1}{\mathcal{H}\eta} \Theta_\ell + \tau' \Theta_\ell. \quad (33e)$$

#### CDM and baryons

$$\delta' = \frac{ck}{\mathcal{H}} v - 3\Phi', \quad (34a)$$

$$v' = -v - \frac{ck}{\mathcal{H}} \Psi, \quad (34b)$$

$$\delta'_B = \frac{ck}{\mathcal{H}} v_B - 3\Phi', \quad (34c)$$

$$v'_B = -v_B - \frac{ck}{\mathcal{H}} \Psi + \tau' R(3\Theta_1 + v_B). \quad (34d)$$

#### Metric perturbations

$$\Phi' = \Psi - \frac{c^2 k^2}{3\mathcal{H}^2} \Phi + \frac{1}{2} [\delta\Omega_{\text{CDM}} + \delta_B\Omega_B + 4\Omega_\gamma\Theta_0], \quad (35a)$$

$$\Psi = -\Phi - \frac{12\mathcal{H}^2}{c^2 k^2} \Omega_\gamma \Theta_2. \quad (35b)$$

We have now removed all spatial dependency from the various quantities which are instead expressed in terms

of the Fourier mode  $k$ . These modes now, instead of representing the spatial distribution, represent a unique spatial scale. Since Fourier modes in general are related to frequency, which is inversely proportional to wavelength, then  $k \sim 1/\lambda$  where  $\lambda$  is the relevant length scale. As such this is a very efficient way to look at what exactly happens at different cosmological scales. One can also relate these various scales to the Horizon to see what scales are causally connected and disconnected by considering the quantity  $k\eta$ . If  $k\eta \gg 1$  then we are working with scales much smaller than the horizon, if  $k\eta \ll 1$  these scales are much larger than the horizon and represent acausal distances. Finally  $k\eta \simeq 1$  is the scale at which the mode relates quantities which are the same magnitude as the horizon.

### 3.1.5. Tight coupling

One particular problem behind the set of differential equations in the very early universe  $\tau' \gg 1$  due to photons and baryons being tightly coupled due to the primordial plasma, making it optically thick.  $\tau \gg 1$  implies that baryons in the early universe only interacts with its close neighbourhood. This is what we call the **tight coupling regime**. This in turn causes the set of differential equations to be numerically unstable. To remedy this we instead attempt to consider a numerically stable approximation for  $\Theta_1 + \frac{1}{3}v_B$  in this regime. Adding together  $3 \times (33b)$  and  $(34d)$  yields

$$[3\Theta_1 + v_B]' = \frac{ck}{\mathcal{H}}(\Theta_0 - 2\Theta_2) + \tau'(1+R)[3\Theta_1 + v_B] - v_B. \quad (36)$$

Taking the next derivative of this, using  $R' = -R$  and  $(34d)$  again to get rid of  $-v_B'$  we arrive at

$$\begin{aligned} [3\Theta_1 + v_B]'' = & -\frac{ck}{\mathcal{H}} \frac{\mathcal{H}'}{\mathcal{H}} (\Theta_0 - 2\Theta_2) + \frac{ck}{\mathcal{H}} (\Theta_0 - 2\Theta_2)' \\ & + (\tau''(1+R) - R\tau')[3\Theta_1 + v_B] \\ & + (\tau'(1+R) - 1)[3\Theta_1 + v_B]' + 3\Theta_1'. \end{aligned}$$

Substituting in the equation for  $\Theta_1'$  and approximating that  $(3\Theta_1 + v_B) \propto \tau'^{-1} \propto \eta$  which holds during radiation domination. This implies that

$$[3\Theta_1 + v_B]'' \approx -\frac{\mathcal{H}'}{\mathcal{H}} [3\Theta_1 + v_B]'$$

Then solving for  $q \equiv [3\Theta_1 + v_B]'$  we arrive at

$$\begin{aligned} q = & -\frac{1}{\tau'(1+R) + \frac{\mathcal{H}'}{\mathcal{H}} - 1} \times \\ & \left[ (\tau''(1+R) + (1-R)\tau')[3\Theta_1 + v_B] \right. \\ & \left. + \frac{ck}{\mathcal{H}} \left( \Psi + \Theta_0' - 2\Theta_2' + \left(1 - \frac{\mathcal{H}'}{\mathcal{H}}\right) (\Theta_0 - 2\Theta_2) \right) \right]. \end{aligned}$$

One can however show that  $\Theta_2' \sim 3\Theta_2 \ll \Theta_0$  during this epoch, thus we can ignore this term. In fact we will ignore the explicit time evolution of all multipoles of higher order than the dipole in this regime. We will however implicitly evolve them as these higher order multipoles do depend on the evolution of  $\Theta_0$  and  $\Theta_1$ . Further we can solve for  $\tau'(1+R)[3\Theta_1 + v_B]$  by using (36) and substitute this into the equation for  $v_B'$  to give us

$$v_B' = \frac{1}{1+R} \left[ R \left( q + \frac{ck}{\mathcal{H}} (2\Theta_2 - \Theta_0 - \Psi) \right) - v_B - \frac{ck}{\mathcal{H}} \Psi \right].$$

With this we arrive at a set of equations which we expect to hold before recombination, summarized in (37). Note however that the equations for  $\Theta_0', \delta', v', \delta_B'$  and  $\Phi'$  remain the same in this regime as they are numerically stable. The equations for  $\Theta_\ell$  with  $\ell \geq 2$  are stated here and come from the initial conditions, to be discussed later.

#### Tight coupling regime

$$\begin{aligned} q \left[ (1+R)\tau' + \frac{\mathcal{H}'}{\mathcal{H}} - 1 \right] \\ = -[\tau''(1+R) + \tau'(1-R)](3\Theta_1 + v_B) \\ - \frac{ck}{\mathcal{H}} \left[ \Psi + \Theta_0' - \left(1 - \frac{\mathcal{H}'}{\mathcal{H}}\right) (2\Theta_2 - \Theta_0) \right], \end{aligned} \quad (37a)$$

$$\begin{aligned} v_B[1+R] = & R \left( q + \frac{ck}{\mathcal{H}} (2\Theta_2 - \Theta_0 - \Psi) \right) \\ & - v_B - \frac{ck}{\mathcal{H}} \Psi, \end{aligned} \quad (37b)$$

$$\Theta_1' = -\frac{1}{3}(q - v_B'), \quad (37c)$$

$$\Theta_2 = -\frac{20ck}{45\mathcal{H}\tau'}\Theta_1, \quad (37d)$$

$$\Theta_\ell = -\frac{\ell}{2\ell+1} \frac{ck}{\mathcal{H}\tau'} \Theta_{\ell-1}, \quad \ell > 2. \quad (37e)$$

### 3.1.6. Inflation

To begin solving the various differential equations we of course need initial conditions. This is done by considering what conditions the universe satisfies once inflation ends.

In the CMB spectra we see today there is seemingly a correlation between the photon temperature fluctuations on acausal scales. Together with this we observationally have a universe which is flat to a very high degree of confidence. This would in turn cause a huge fine tuning problem in the early universe as the “flatness” of the universe would increase over time implying that it must have been much smaller in the past. To explain these observational

phenomena we consider a universe which expanded exponentially for a short time frame in the very early universe; this is what is known as inflation. This event would allow for an initially non-flat universe together with allowing for relatively large scales to be within the horizon at very early times to allow for interactions, causing correlations between them. Then moments later the universe exponentially expands causing the universe to appear flat on smaller scales (such as the observable universe today) and would drive correlations between what would today seem like acausal scales.

We assume that inflation is driven by a scalar quantum field  $\phi$  which we call the inflaton field. We make the assumption that we can model the collection of inflaton as a perfect fluid along with assuming that the early universe was dominated by this inflaton field. With these assumptions the Friedmann equations yield that the inflaton must have an equation of state such that  $p < -\rho/3$ , i.e. the inflaton field must have a sufficiently negative pressure. By considering the Lagrangian for the inflaton field together with its stress-energy tensor: [4]

$$T^\mu{}_\nu = g^{\mu\rho} \frac{\partial\phi}{\partial x^\rho} \frac{\partial\phi}{\partial x^\nu} - \delta^\mu_\nu \left[ \frac{1}{2} g^{\rho\sigma} \frac{\partial\phi}{\partial x^\rho} \frac{\partial\phi}{\partial x^\sigma} + V(\phi) \right],$$

one can obtain the following relations for the energy density and pressure:

$$\begin{aligned} \rho_\phi &= \frac{1}{2} \left( \frac{d\phi}{dt} \right)^2 + V(\phi), \\ p_\phi &= \frac{1}{2} \left( \frac{d\phi}{dt} \right)^2 - V(\phi), \end{aligned}$$

where  $V(\phi)$  is the potential energy of the inflaton field. The restriction on the equation of state suggests that the inflaton field must have more potential energy than kinetic energy. In order to avoid a rapid phase transition of the inflaton field s.t. we don't mess with potential observations, we then consider a slow roll down the potential.

To account for the small fluctuations in the CMB spectra we assume that these are initially caused by tiny quantum fluctuations of the inflaton fields. To do this we write

$$\phi(t, \mathbf{x}) = \phi^0(t) + \delta\phi(t, \mathbf{x}),$$

where  $\phi^0$  is the equilibrium of the field and  $\delta\phi$  is a small perturbation, not to be confused with the perturbed number density for CDM. To proceed from here we consider a conserved quantity during throughout the inflationary epoch:

$$\xi = -\frac{ik^i \delta T_i^0 H}{k^2(\rho + p)} - \Psi, \quad (38)$$

where  $k_i$  is the Fourier mode. At a time  $t_i$  before inflation we assume that the universe is perfectly FLRW, i.e.  $\Phi = \Psi = 0$ , one arrives at

$$\xi(t_i) = -aH \frac{\delta\phi}{\dot{\phi}},$$

where we temporarily refer to  $\dot{\phi} \equiv \frac{d\phi}{dt}$  instead of w.r.t.  $\eta$ . Using the conserved quantity again at  $t_f$  representing the end of equation where we now assume that radiation domination has begun then we have

$$\xi(t_f) = -\frac{3}{2}\Psi.$$

Equating the two we then have an initial value for  $\Psi$  at the time where the mode  $k$  crosses the horizon:

$$\Psi = \frac{2}{3} \mathcal{H} \frac{\delta\phi}{\dot{\phi}} \Big|_{\mathcal{H}=k}. \quad (39)$$

The FRLW perturbed Klein-Gordon equation for the inflaton can then be found to be:

$$\delta\ddot{\phi} + 2\mathcal{H}\delta\dot{\phi} + k^2\delta\phi = 0.$$

Quantizing  $\phi$  and solving this damped harmonic oscillator equation then allows us to relate  $\delta\phi$  to all the other quantities.

### 3.1.7. Initial conditions

We can now determine initial conditions to allow us to solve the full system. We have made a connection between the Newtonian scalar  $\Psi$  and the perturbations in the inflaton field  $\delta\phi$ . As such, all that remains is to connect  $\Psi$  to the rest of our parameters. To do this we make the assumptions that we have either adiabatic initial conditions, i.e. that the density fluctuations are present at the end of inflation, or that we have isocurvature perturbations, i.e. that fluctuations are generated from causal interactions of matter. For adiabatic perturbations, the number density of each species is the same everywhere:

$$\frac{n_i}{n_\gamma} = \frac{\bar{n}_i}{\bar{n}_\gamma},$$

where  $i$  represents the particle type. Since  $\bar{\rho}_i(a) \propto a^{-3(1+\omega_i)}$  [8] we have that

$$\rho_i(x, a) = \bar{\rho}_i(a + \delta a(x)) \simeq \bar{\rho}_i(a)(1 - 3a^{-1}(1 + \omega_i)\delta a).$$

As such we have that  $\delta_i(x, a) = -3a^{-1}(1 + \omega_i)\delta a$  which then yields that, for any species  $i, j$ , the following relation holds:

$$\frac{\delta_i}{1 + \omega_i} = \frac{\delta_j}{1 + \omega_j}.$$

Using this on our various particle species we have that  $4\Theta_0 = \delta_B = \delta$ . Further, connecting this to  $\Phi$  and  $\Psi$  we have that at very early times:

$$\begin{aligned} k\eta &\simeq \frac{ck}{\mathcal{H}} \ll 1 \leftrightarrow k \ll \mathcal{H}, \\ \tau &\gg 1 \quad |\tau'| \gg 1. \end{aligned}$$



The first is necessary ensure that there exist causally disconnected regions in the early universe and the second is already established in section 2. Noting that the metric perturbation evolve very slowly outside the horizon, we have  $\Phi \approx \Psi \approx 0$ . The Poisson equation then yields  $2\Theta_0 \simeq -\Psi$ . This is then used to connect all the various particle types to  $\Psi$  and hence  $\Phi$ . Next we have the velocity equations. The equation for the CDM velocity can be rewritten:

$$(ve^x)' = -\frac{cke^x}{\mathcal{H}}\Psi.$$

Integrating this and throwing away an exponentially damped term  $Ce^{-x}$  we arrive at

$$v = -\frac{ck}{2\mathcal{H}}\Psi.$$

Similar arguments work for baryons and  $\Theta_1$ . The arguments for the general  $\Theta_\ell$  is a little more involved, but an analytical approximation yields: [1]

$$\Theta_\ell \simeq -\frac{\ell}{2\ell+1} \frac{ck}{\mathcal{H}\tau'} \Theta_{\ell-1}, \quad \ell > 2.$$

Here we can see that  $\Theta_{\ell+1} \propto \tau'^{-\ell}$  for  $\ell > 0$ , as such this implies that  $\Theta_\ell \gg \Theta_{\ell+1}$  since  $\tau' \gg 1$  which justifies the assumptions made in the tight coupling regime.

Now that everything is related to  $\Phi$  and  $\Psi$  we decide to introduce a normalization for computational purposes. Since the set of equations, even in the full regime, is linear we can freely choose the normalization of the system at this stage. As such one cannot make take any physical meaning from the numerical values of any of the quantities from here on and only their relative quantities until we insert this factor back later in section 4. Note that this includes removing any phase from the various Fourier transformed quantities, but, as we will see in section 4, we are only interested in the absolute value squared.

For a mode outside the horizon in the radiation era we have that

$$\xi \simeq \Phi - \frac{1}{2}\Psi,$$

where  $\xi$  was defined (38). The relation of the two potentials is given by [4]

$$\Phi + \Psi \simeq 0,$$

if one ignores neutrinos. If we choose the normalization of  $\xi = 1$  then which yields  $\Phi \simeq -\Psi \simeq \frac{2}{3}$ . Rewriting everything in terms of  $\Psi$  we have the full set of initial conditions summarized in (40).

### Initial conditions

$$\Psi = -\frac{2}{3}, \quad (40a)$$

$$\Phi = -\Psi, \quad (40b)$$

$$\delta = \delta_B = -\frac{3}{2}\Psi, \quad (40c)$$

$$v = v_B = -\frac{ck}{2\mathcal{H}}\Psi, \quad (40d)$$

$$\Theta_0 = -\frac{1}{2}\Psi, \quad (40e)$$

$$\Theta_1 = \frac{ck}{6\mathcal{H}}\Psi, \quad (40f)$$

$$\Theta_2 = -\frac{20ck}{45\mathcal{H}\tau'}\Theta_1, \quad (40g)$$

$$\Theta_\ell = -\frac{\ell}{2\ell+1} \frac{ck}{\mathcal{H}\tau'} \Theta_{\ell-1}, \quad (40h)$$

$\ell > 2.$

### 3.2. Implementation details

We began by implementing logarithmically spaced values for  $k \in [5 \cdot 10^{-5}, 0.3]/\text{Mpc}$ . Then we solved the tight coupling (TC) system with the given initial conditions. The chosen number of multipoles in this section was  $\ell_{\text{max}} = 8$ . For the TC system we included all the  $\Theta_\ell$  but only explicitly evolved the monopole and dipole as explained in the theory section. However we still implicitly updated the values for  $\ell \geq 2$  with the equations for their initial conditions supplied by the new values for  $\Theta_0$  and  $\Theta_1$  which recursively affects larger  $\ell$ . If any of the following conditions are true we then exit out of the TC regime:

$$|\tau'| < 10, \quad |\tau'| < 10 \frac{ck}{\mathcal{H}}, \quad x > -8.3.$$

The necessity of requiring that  $|\tau'|$  is relatively low can be seen from (33a). The particular value of  $\tau'$  to exit the TC regime is not of particularly high importance, and some check with larger  $\tau'$  values were done to verify this. The next condition comes from imposing different TC regimes at different scales. A proper justification for this can be found in [9]. The final condition is a balance between speed and change in data. Ideally one would want to exit TC as soon as possible, but it turns out that we can keep going for quite some time without any noticeable effects, massively speeding up the computation times.

Once one of these conditions are satisfied, we saved the time in which this occurred, and began to solve the full system. The initial conditions for the full system were supplied by the final values for the TC solution. The solutions are then splined and converted over to data files to be analyzed in Python. We then chose 3 values for  $k = \{0.1, 0.01, 0.001\}/\text{Mpc}$  which have been chosen to assess large, intermediate and small scales respectively.

For the above mentioned scales we plotted the density and velocity perturbations for CDM, baryons and photons. Further we made some graphs related to quadrupole moment  $\Theta_2$  and the Newtonian potentials  $\Phi$  and  $\Psi$  to be discussed in the next section.

### 3.3. Results

The considered the modes, as previously mentioned, are  $k = \{0.1, 0.01, 0.001\}/\text{Mpc}$ . Since we are generally interested in when causal physics begins to occur, the time at which  $k\eta \sim 1$  is of physical significance. As such Table III summarizes the times in which one should expect to see the data be affected by any potential gravitational wells and radiation pressure at the given scales. Note that when photons and baryons are tightly coupled

Table III.  $x$  values for when  $k\eta \sim 1$  and  $k\eta \sim 1/\sqrt{3}$  for the different scales. The latter is used for estimating the particle horizon for photons and baryons following previous discussion regarding their sound horizon.

Mode [ $\text{Mpc}^{-1}$ ]	$x_{\text{CDM}}$	$x_{\gamma, \text{B}}$
$k = 0.1$	-11.0	-11.6
$k = 0.01$	-8.5	-9.1
$k = 0.001$	-5.2	-6.1

we expect them both to follow the radiation domination sound horizon instead of the particle horizon. Here we can already see that the large scales should remain unaffected by the radiation pressure due to recombination already having occurred, and hence the universe is neutral by the time causal physics enters. Note that both of these are just approximations as we only really use  $k\eta \sim 1$  to separate the times for when  $k\eta \ll 1$  where one should not expect any interactions, and  $k\eta \gg 1$  for when one should expect to see them. As we will see later, in general, the causal physics begins to enter before the criteria that  $k\eta \gtrsim 1$ .

As mentioned in the initial conditions section, we have stripped the scaling from all the various quantities. As such one cannot give any meaning to the exact value of any of the quantities as this has been factored out. However we can still interpret the relative changes in the various quantities over time. In section 4 we will reintroduce this factor which we have gotten rid of to probe the CMB power spectrum.

#### 3.3.1. Matter overdensity and bulk velocity

We begin by considering how the matter density fluctuations and velocities of CDM and baryons change over time, depicted in Fig. 11. Overdensities for these particles are primarily created by gravity pulling matter together once the particle horizon reaches the given scale.

As such, we consider Table III for when we expect to see these overdensities begin to grow at the various scales, shown as the colored vertical lines.

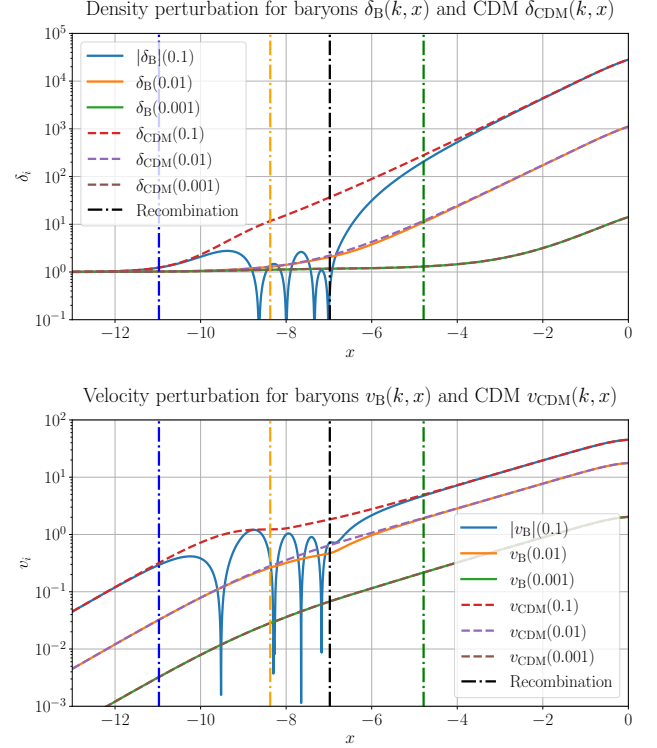


Fig. 11.  $\delta_B, \delta_{\text{CDM}}$  and  $v_B, v_{\text{CDM}}$  as a function of  $x$  at modes  $k = 0.1/\text{Mpc}$ ,  $k = 0.01/\text{Mpc}$  and  $k = 0.001/\text{Mpc}$  for small, intermediate and large scales respectively. The dot-dashed blue, yellow and green lines correspond to horizon crossing for the small, intermediate and large scale modes respectively.

One thing to note here is that from (30, 31), bringing these differential equations to our time variable  $x$ , Fourier transforming and setting  $\Phi' = 0$  (which we will see later is a reasonable assumption at certain times), these equations essentially just sets  $v \propto \delta'$  for both baryons and CDM given a slow enough expansion rate. This of course implies that the velocity acts as the time derivative of  $\delta$  given that the potential  $\Phi$  does not evolve. This is manifest for certain ranges of  $x$  in Fig. 11, with some deviations in the range  $-12 < x < -6$ .

We see that for smaller scales, both CDM and baryons begin to cluster at  $x \approx -12$  and their velocities follow one another with equal velocities until  $x \approx -11$ . This is contrary to what Table III suggests, seemingly implying that acausal clustering has occurred, but a reminder that this criteria is a simplification and as such one does not expect this to be completely accurate. A more accurate indication would require considering the sound horizon at the given time. Prior to this there is no clustering whatsoever due to the horizon being much smaller than the scale. Since this is during the radiation epoch, the velocity of all scales can be seen to increase the same amount.

The overdensities then continue follow one another until a critical point at around  $x \approx -10$ . This corresponds to when the outward pressure from clustering photons, as we are in radiation domination at this time, begin to work as a repulsive mechanism to counteract the gravitational pull. However, CDM still continue to cluster up as they are singlets under electromagnetism and continue to create increasingly deep gravitational wells.

At  $x \approx -9$  we can see that there is an equilibrium between the gravitational pull and the outwards pressure from photons. As the gravitational wells from CDM grow deeper, the baryons are pulled back again, creating the oscillatory pattern we see here. We note that is it the absolute value of  $\delta_B$  and  $v_B$  which is being plotted such that it fits on a logarithmic plot. Hence, each dip corresponds to the time where  $\delta_B$  and  $v_B$  switch signs, changing from an overdensity to a lack of overdensity. Reminder that the plots are the Fourier transform of the various quantities. As such the harmonic behavior we see here corresponds to propagating waves of matter density in real space. During this time we can see that this in fact does have an effect on CDM. There is a noticeable drop in their velocity as they begin to follow the baryons due to their gravitational interactions. The counterplay between the combined gravitational pull from matter and the outwards radiation pressure then proceed to play a role for quite some time until recombination occurs. Before this however, one sees that the velocity growth begins to change its power law as we enter matter domination. This causes the universe to accelerate faster, causing velocities to increase at a slower pace. Later, as the number of free electrons in the universe rapidly decay, the outward pressure from the photons effectively ceases as recombination is in the process of occurring.

The universe then becomes electrically neutral once atoms begin to form, allowing photons to free streaming and no longer impose the outward pressure. This in turn causes the overdensities to begin to grow unbounded from here until they eventually get caught by the gravitational wells caused by CDM. These gravitational wells then begin to snowball and scale exponentially w.r.t.  $x$ . This continues until the acceleration caused by dark energy slows down the overdensity and velocity growth as the exponential growth slightly flattens. This effect can be seen on all scales.

For the intermediate scale we can see that there is no overdensity in the graph until about  $x \approx -9$  and their velocities remain the same until roughly  $x \approx -8.5$ . Once again checking Table III, there is a reasonable agreement between the plot and the expected time for causal physics to enter. As with the smallest scale, the gravitational pull of CDM and baryons begin to form overdensities. It then comes to a point where the difference between the two become visible at  $x \approx -7.5$ . Again this is due to the outward repulsion of photons, but to a much smaller extent as the scale is too large for the radiation pressure to have a large effect. At this point the number of free electrons is also relatively low, causing photons to not

interact as often. Due to there not being much time until recombination, these oscillations do not have time to manifest, causing the repulsions to stop and thus only allowing for a singular small oscillation. As with the small scale, the baryons begin to form overdensities together with CDM until they once again coincide at a later time.

At the largest scale which we consider, one can see that there is in fact no oscillations whatsoever. This was already expected from the previous discussion under Table III due to the universe being electrically neutral. Hence one does not expect to see any oscillations whatsoever at these scales and, from this point of view, the baryons simply act as CDM throughout.

### 3.3.2. Photon overdensity and bulk velocity

We present the photon overdensity and velocity for all the modes we are considering in Fig. 12. As mentioned previously we have the relations  $\delta_\gamma = 4\Theta_0$  and  $v_\gamma = -3\Theta_1$ . The first of these relations can be justified physically as the photon monopole is a measure of the average photon temperature, which can be related to photon overdensities. A derivation for the factor of 4 can be found in [1]. The latter can be compared to the observation of the CMB spectra as one would see from a non-comoving observer. If one has a velocity w.r.t. the CMB one would see a strong dipole moment depending on the velocity of said observer. As such it is not hard to make the justification that the dipole moment should be related to the velocity.

To gain a clearer understanding of the correlation between the overdensity and velocity of photons and baryons, Fig 13, 14 and 15 show  $\delta_\gamma$  and  $v_\gamma$  compared to  $\delta_B$  and  $v_B$  for the modes  $k = \{0.1, 0.01, 0.001\}/\text{Mpc}$  respectively.

As expected from the discussion of the tight coupling regime, the two quantities are deeply related at all scales. Here one sees that even past the tight coupling regime, the two continue to follow one another at all scales, however the overdensities formed by the photons is noticeable larger at all scales. This can be seen from (40) as we begin with  $\delta_\gamma = 4\Theta_0 = -2\Psi$ , and  $\delta_B = -\frac{3}{2}\Psi$  the ratio  $\delta_\gamma/\delta_B = 4/3$  exactly as we see in the figure at early times.

For the smallest scale in depicted in Fig. 13 one sees that after horizon crossing, the densities for both photons and baryons begin to grow due to gravitational wells. Later this reaches a peak as the radiation pressure causes an unstable equilibrium at around  $x \approx -9.5$ . This radiation pressure then drags the baryons along with the photons causing a propagation of the overdensity in the real space. At  $x \approx -8.5$  the radiation pressure begins to be dominated by the gravitational wells caused by dark matter as previously discussed. This then continues a couple more times before recombination occurs. Once this happens, a near instantaneous decoupling between the photons and baryons can be seen, and baryons are left

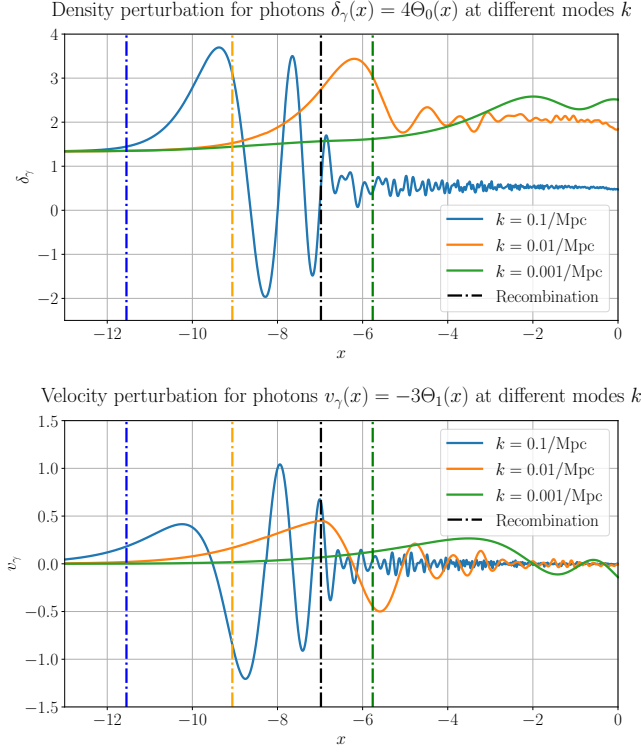


Fig. 12.  $\delta_\gamma$  and  $v_\gamma$  as a function of  $x$  at modes  $k = 0.1/\text{Mpc}$ ,  $k = 0.01/\text{Mpc}$  and  $k = 0.001/\text{Mpc}$  for small, intermediate and large scales respectively. The dot-dashed blue, yellow and green lines correspond to horizon crossing for the small, intermediate and large scale modes respectively and the black dot-dashed line corresponds to the time of recombination.

to freely cluster in the ever-growing gravitational wells. From here on the photons are effectively free as neutral atoms form and only experience mild oscillations about the average density fluctuations which we can clearly see is not at 0. Note that the effective photon temperature perturbation is in fact  $\Theta_{\text{eff}} = \Theta_0 + \Psi$  [1]. As such one does not expect the oscillations to oscillate about 0 on these scales, but instead that  $\Theta_{\text{eff}}$  does.

In the intermediate scale shown in Fig. 14 we again see much of the same physics as for the smallest scale. As in the discussion for the baryons and CDM, the clustering begins to manifest shortly before the horizon crossing. Here one can more readily see that the clustering occurs until a bit after recombination, but does not have time to cause the oscillatory motion for the baryons that we saw on the smallest scale. The photon density then dips down again until it reaches its equilibrium. Note that when the universe begins to accelerate, a noticeable second dip in the photon density occurs. This is once again due to dark energy domination occurring and is more prominent on larger scales.

The largest scale that we consider in Fig. 15 the build-up starts much later. Unlike the prior two scales, the velocities of the baryons and photons do not immediately

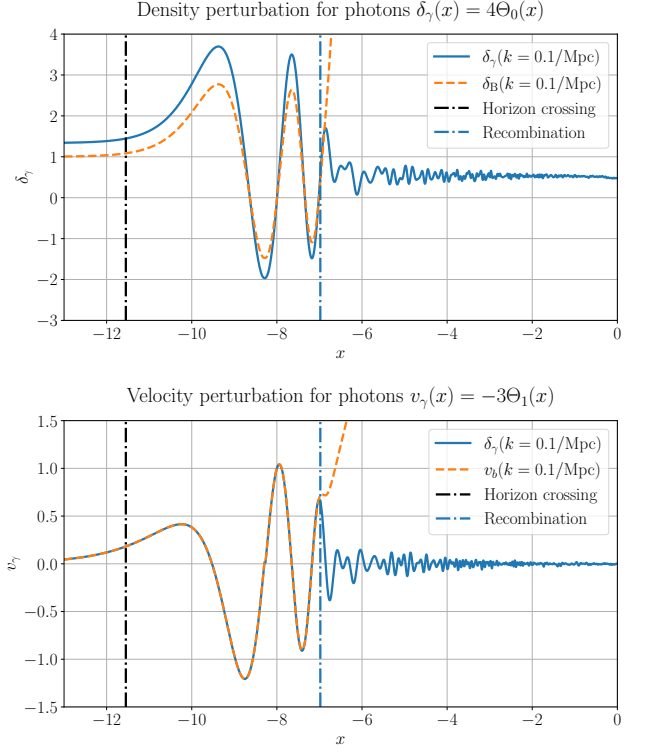


Fig. 13.  $\delta_\gamma$  and  $v_\gamma$  as a function of  $x$  compared to  $\delta_B$  and  $v_B$  at the mode  $k = 0.1/\text{Mpc}$ .

decouple to the same extent after recombination at these scales. But we can still see that there is a noticeable difference in the two past this point. The oscillations in Fourier space after the photon density peak is then much slower here compared to the previous cases due to the propagating waves travelling at velocity  $\sim c$  in real space moving much slower relative to the size of the scale.

Next we consider the evolution of the quadrupole moment  $\Theta_2$  for the considered length scales depicted in Fig. 16.

One thing to note is that in the derivation of the TC system, an assumption that the early universe is without anisotropic stress, meaning that the stress energy tensor is invariant under spatial rotations. As a consequence, given our conventions, the EFE sets  $\Phi = -\Psi$ . In the full system this is however not necessarily the case. With this in mind, considering (35b), we see that in this model, anisotropic stress is then deeply related to both  $\Omega_\gamma$  and  $\Theta_2$ . In the era where  $\Theta_2 = 0$  we will then expect the sum  $\Phi + \Psi = 0$  which we will come back to later.

For the smallest scale we see that the oscillations in Fourier space begin quite late in comparison to when one would expect to see effects due to the horizon crossing. A small oscillation can then be seen to build up rather quickly until it peaks shortly after recombination. As such the anisotropy that one would expect from photons in the CMB spectra should be rather large at these scales. This also implies that the assumption that  $\Phi = -\Psi$  is

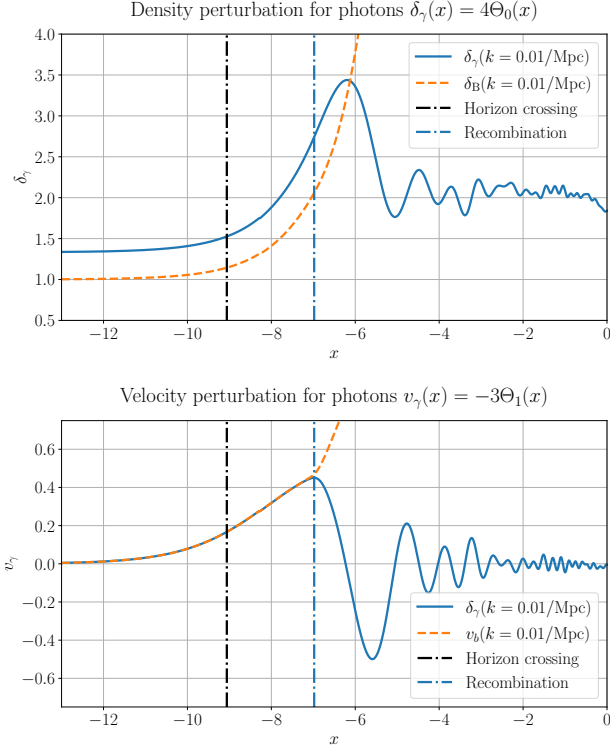


Fig. 14.  $\delta_\gamma$  and  $v_\gamma$  as a function of  $x$  compared to  $\delta_B$  and  $v_B$  at the mode  $k = 0.01/\text{Mpc}$ .

less convincing at this time, something that we will see later. The oscillations then quickly fall off as time evolves past recombination, but are still noticeable compared to before TC ends.

For the intermediate scale we see that the oscillations begin much faster when compared to the particle horizon. As in the small scale the oscillations quickly build up, peaking at about  $x \approx -5.5$ . This once again signifies anisotropies. As with the small scales, the oscillation decay, but albeit at a much slower pace.

At the largest scale we see that the main oscillation starts up before the expected horizon crossing. It then has its absolute extremum at  $x \approx -3.5$  and continues its oscillatory motion until present day.

### 3.3.3. Gravitational potentials

Considering the potentials  $\Phi$  and  $\Psi$  as a function of time for the modes  $k = \{0.1, 0.01, 0.001\}/\text{Mpc}$  shown in Fig. 17 where the potential  $\Phi$  is given in the top figure and the sum  $\Phi + \Psi$  is given in the lower figure.

At early times we see that the potential  $\Phi$ , and thus the potential  $\Psi$  are constant as expected due to the horizon being much smaller than the considered modes. As can be seen from the second figure,  $\Phi = -\Psi$  at early times justified by the fact that the quadrupole moment  $\Theta_2 = 0$  at this time.

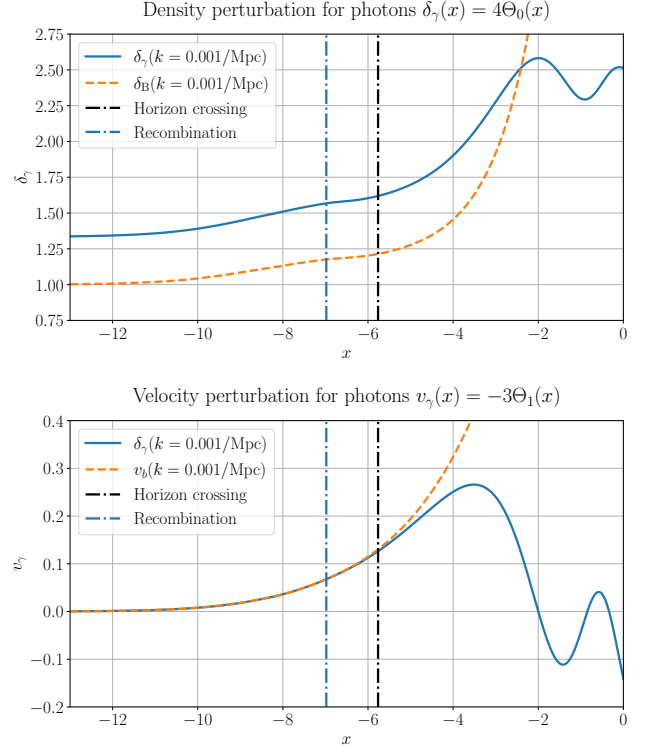


Fig. 15.  $\delta_\gamma$  and  $v_\gamma$  as a function of  $x$  compared to  $\delta_B$  and  $v_B$  at the mode  $k = 0.001/\text{Mpc}$ .

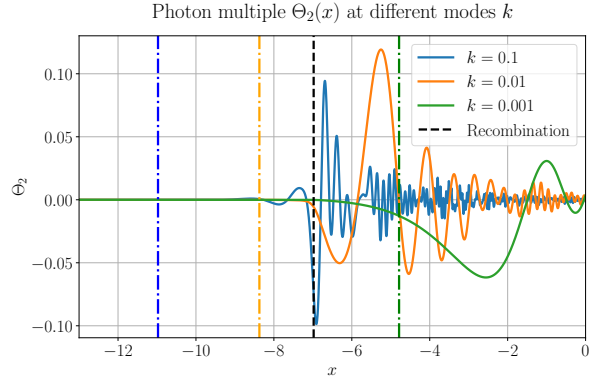


Fig. 16. Time evolution of the photon quadrupole  $\Theta_2$  at modes  $k = 0.1/\text{Mpc}$ ,  $k = 0.01/\text{Mpc}$  and  $k = 0.001/\text{Mpc}$  for small, intermediate and large scales respectively. The dot-dashed blue, yellow and green lines correspond to horizon crossing for the small, intermediate and large scale modes respectively.

At later times, as the particle horizon expands, the smaller scales, corresponding to the higher value of the modes, enter the horizon. As indicated in Table III for small scales, it is expected that causal physics will begin to play a role at around  $x \approx -11.0$ . In turn this allows for radiation pressure, which is dominant at this time, to effectively counteract the gravitational poten-

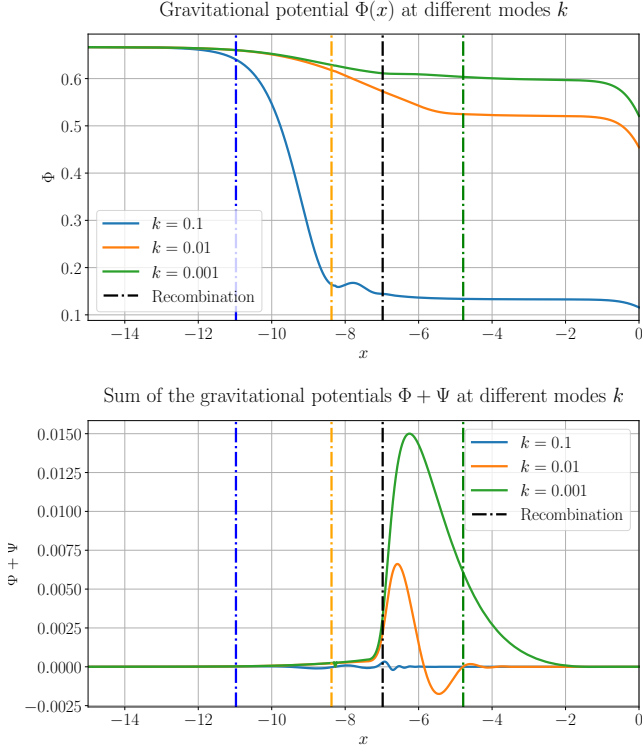


Fig. 17. Time evolution of  $\Phi(x)$  along with the sum  $\Phi(x) + \Psi(x)$  at modes  $k = 0.1/\text{Mpc}$ ,  $k = 0.01/\text{Mpc}$  and  $k = 0.001/\text{Mpc}$  for small, intermediate and large scales respectively. The dot-dashed blue, yellow and green lines correspond to horizon crossing for the small, intermediate and large scale modes respectively.

tial and prevents over-densities to form in the primordial baryon-photon plasma. After a large drop in  $\Phi$ , it then begins to oscillate in a damped fashion which comes from the back-and-forth between radiation pressure and induced gravitational wells from CDM and baryons. This is clearly seen at smaller scales but the effect is massively suppressed at larger scales. One can also notice that the sum  $\Phi + \Psi$  barely changes at these small scales, suggesting that the anisotropies at these scales are relatively small, but there are still some small oscillations around recombination as could be expected from Fig. 16. Finally the potential  $\Phi$  flattens out during matter domination, which is to be expected for  $k \gtrsim 0.1/\text{Mpc}$  which agrees with our result.

For the intermediate scales we see that the drop-off of the potential starts later, once again expected from Table III and is much slower compared to smaller scales. The drop-off then remains constant with respect to  $x$  during recombination until, as before, it flattens out to a constant during matter domination. The anisotropies, in the lower figure, are noticeable at these scales.

The large scale mode begins to drop at roughly the same time as intermediate scales, but once again slower than the others. Table III seems to imply that this cannot

causally happen at this time. Analytically one can find the expected change to the potential to be a factor of 9/10 as the universe transitions from radiation to matter domination [1] which seems to agree with the green line in the top figure. Further there is a much larger relative difference between the two potentials, due to the  $k^{-2}$  dependence in the anisotropy term.

For all scales we see that during matter domination, the gravitational potentials flatten out at every scale. Naively one would expect it to increase in this period as all matter is effectively neutral and thus things would collapse together gravitationally, but the expansion of the universe works as a counteractive force against gravitational wells, and thus it remains roughly constant at all scales. In the lower figure we see that at late times the sum of the Newtonian scalars once again satisfy  $\Phi = -\Psi$ . Again referring (35b) we have that  $\Omega_\gamma \approx 0$  past a certain point. As such, even with the continuing oscillatory motion of the quadrupole moment, the anisotropies are cancelled out by the lack of radiation at late times. At last one sees a drop-off, where the magnitude of this drop-off is seemingly proportional to the scale, as the universe begins to expand due to dark energy beginning to dominate. This makes sense physically as when the repulsive nature of dark energy takes over, it will expand the distance between massive objects, causing the gravitational potentials to fall off.

### 3.4. Summary

In this section we first solved the approximated tight coupling system and exited this system before our approximations broke down. We then switched over to the full system up to the given  $\ell_{\text{max}} = 7$ . Three particular modes, each representing a given scale, were then chosen and discussed in detail for the various quantities.

## 4. THE CMB AND MATTER POWER-SPECTRA

Now that we have solved the background cosmology, retrieved relevant data from the era of recombination and solved the perturbations on the background cosmology we are finally in a position to compute the CMB power spectrum. Since we have already calculated  $\Theta_\ell(k, x)$ , all we need to do to find the coefficients is to read in this data at time  $x = 0$ . One problem we have is that since we only computed to  $\ell_{\text{max}} = 7$  in the prior section, and we would like to probe smaller regions than this, e.g.  $\ell_{\text{max}} = 2000$ . This would be incredibly slow with our code so we need to consider a new technique to compute this. To do this we use the so-called line-of-sight integration technique to be introduced in the theory section.

### 4.1. Theory

#### 4.1.1. Line-of-sight integration

The idea behind line-of-sight (LOS) integration is that instead of performing a multipole expansion on equation (27) we begin by integrating the equation for  $\Theta$  and perform the multipole expansion afterwards. Doing this one arrives at

$$\Theta(k, \mu, \eta_0) = - \int_0^{\eta_0} \left[ \dot{\Phi} + ik\mu\Psi + \dot{\tau} \left( \Theta_0 + i\mu v_B - \frac{P_2}{2} \Theta_2 \right) \right] \times e^{ik\mu(\eta - \eta_0) - \tau} d\eta$$

where  $\eta_0 \equiv \eta(x=0)$ . Here we can switch out any factors of  $\mu$  with a derivative w.r.t.  $\eta$  and the necessary coefficients. Expanding in multipoles, integrating over  $\mu$  and using the definition of Bessel functions  $j_\ell$ :

$$\frac{i^\ell}{2} \int_{-1}^1 d\mu P_\ell(\mu) e^{ik\mu(\eta - \eta_0)} = j_\ell[k(\eta_0 - \eta)],$$

we arrive at

$$\Theta_\ell(k, \eta_0) = \int_0^{\eta_0} d\eta S(k, \eta) j_\ell[k(\eta_0 - \eta)], \quad (41)$$

where the source function  $S(k, \eta)$  is defined as

$$S(k, \eta) = \tilde{g} \left[ \Theta_0 + \Psi + \frac{1}{4} \Theta_2 \right] + e^{-\tau} \left[ \dot{\Psi} - \dot{\Phi} \right] - \frac{1}{k} \frac{d}{d\eta} (\tilde{g} v_B) + \frac{3}{4k^2} \frac{d^2}{d\eta^2} (\tilde{g} \Theta_2).$$

Rewriting (41) in terms of  $x$  we then have

$$\Theta_\ell(k, x=0) = \int_{-\infty}^0 dx \tilde{S}(k, x) j_\ell[k(\eta_0 - \eta)], \quad (42)$$

where the source function in terms of  $x$  and in SI units now reads

$$\tilde{S}(k, x) = \tilde{g} \left[ \Theta_0 + \Psi + \frac{1}{4} \Theta_2 \right] + e^{-\tau} [\Psi' - \Phi'] - \frac{1}{ck} \frac{d}{dx} (\mathcal{H} \tilde{g} v_B) + \frac{3}{(2ck)^2} \frac{d}{dx} \left[ \mathcal{H} \frac{d}{dx} (\mathcal{H} \tilde{g} \Theta_2) \right], \quad (43)$$

which is what we will be using. For reference, the final term of the source function expanded yields

$$\begin{aligned} \frac{d}{dx} \left[ \mathcal{H} \frac{d}{dx} (\mathcal{H} \tilde{g} \Theta_2) \right] &= \tilde{g}'' \mathcal{H}^2 \Theta_2 + \tilde{g}' (3\mathcal{H} \mathcal{H}' \Theta_2 + 2\mathcal{H}^2 \Theta_2') \\ &+ \tilde{g} (\mathcal{H}'' \Theta_2 + \mathcal{H} \mathcal{H}'' \Theta_2 + 3\mathcal{H} \mathcal{H}' \Theta_2' + \mathcal{H}^2 \Theta_2''). \end{aligned}$$

Now we can easily see that the only quantities which we need to calculate arbitrarily high  $\ell$ 's are ones which we have already calculated in the previous sections together with the corresponding Bessel functions  $j_\ell$ .

#### 4.1.2. CMB power spectrum

With a nice computational trick in hand what remains is to translate the  $\Theta_\ell$  into more convenient observables which we can measure. In order to do this from our various computed quantities we first recall the definition of the spherical harmonics transform of the CMB temperature

$$T(\hat{n}) = \sum_{\ell=0}^{\infty} \sum_{m=-\ell}^{\ell} a_{\ell m} Y_{\ell m}(\hat{n})$$

where  $\hat{n}$  is the direction in the sky,  $Y_{\ell m}$  are the spherical harmonics and  $a_{\ell m}$  are their coefficients. Since inflation predicts initial perturbations to be Gaussian random fields, the spherical harmonic coefficients  $a_{\ell m}$  must also satisfy this. Thus we define the variance of these coefficients  $C_\ell$  to be

$$C_\ell \delta_{\ell\ell'} \delta_{mm'} \equiv \langle a_{\ell m}^* a_{\ell' m'} \rangle,$$

where  $C_\ell$  is the **angular power spectrum**. Note here that since the universe is approximately isotropic we must have the same power spectrum in the various directions; as such we average over  $m$  and drop the subscript. For each fixed  $\ell$ , every  $a_{\ell m}$  contain the same variance and there are  $2\ell + 1$  possible values for  $m$ . Thus to estimate  $C_\ell$  from a given measurement we can estimate the power spectrum as

$$\hat{C}_\ell = \frac{1}{2\ell + 1} \sum_{m=-\ell}^{\ell} |a_{\ell m}|^2.$$

Up until now our theory has been formulated in terms of an ensemble average; however we only have one manifestation of this ensemble to perform measurements on, namely our universe. Due to this, simple statistics then tell us that we will have a large uncertainty on the angular power spectrum for low  $\ell$ 's. This can be easily understood by just considering that for e.g.  $\ell = 2$  we only have 5 patches in the sky to work with, thus we may only have 5 data points which will lead to a large uncertainty. This inescapable fact leads to the notion of **cosmic variance**. The variance of this uncertainty is given by [1]

$$\frac{\text{Var}(C_\ell)}{C_\ell^2} = \frac{2}{2\ell + 1},$$

which comes from the  $a_{\ell m}$  as being Gaussian distributed, implying that  $C_\ell$  must be  $\chi^2$  distributed leading to the variance  $2(2\ell + 1)$ .

Next to actually calculate the angular power spectrum we simply square the  $\Theta_\ell$ , multiply with the primordial power spectrum  $P_{\text{prim}}$  and integrate over all  $k$ . Reminder here that in the previous section we normalized all our quantities, thus we need to bring back the normalization



constant which we factored out, i.e.  $P_{\text{prim}}$ . Doing this yields

$$C_\ell = \frac{2}{\pi} \int dk k^2 P_{\text{prim}}(k) \Theta_\ell^2(k). \quad (44)$$

An in-depth derivation can be found in [1]. The final piece of the puzzle is then to find out what form  $P_{\text{prim}}$  takes. It turns out that most inflation models, including the one we have used here, predict a so-called Harrison-Zel'dovich spectrum [1]. What this implies is that we can write the primordial power spectrum on the form

$$\frac{k^3}{2\pi^2} P_{\text{prim}}(k) = A_s \left[ \frac{k}{k_{\text{pivot}}} \right]^{n_s-1}.$$

Here  $n_s \sim 0.96$  is the spectral index of scalar perturbation,  $A_s$  which is the scalar amplitude of primordial perturbations set up by inflation and  $k_{\text{pivot}}$  is the necessary scale s.t. the amplitude is equal to the observed value of  $A_s$ . For reference, our universe has  $A_s \sim 2 \cdot 10^{-9}$  which implies that we have a pivot scale  $k_{\text{pivot}} \sim 0.05/\text{Mpc}$  [1]. Thus the final expression for the CMB power spectrum that we will use is

$$C_\ell = 4\pi \int_0^\infty dk \frac{A_s}{k} \left[ \frac{k}{k_{\text{pivot}}} \right]^{n_s-1} \Theta_\ell^2(k). \quad (45)$$

Another simple yet important observable to which we can calculate with out data is the matter power spectrum:

$$P_M(k, x) = |\Delta_M(k, x)|^2 P_{\text{prim}}(k), \quad (46)$$

where

$$\Delta_M(k, x) \equiv \frac{2(ck)^2 e^x}{3\Omega_{M0} H_0^2} \Phi(k, x).$$

The matter power spectrum describes the correlation of the matter density fluctuations at a given scale. To explain the data more qualitatively we will also make use of the equality scale

$$k_{\text{eq}} = \mathcal{H}(x_{\text{eq}})/c,$$

which corresponds to the mode which enters the horizon at the time of radiation-matter equality.

## 4.2. Implementation details

We began by computing the source function in (43) with the previously computed quantities. Note that this was implemented together with the script in section 3 with the same  $k$  and  $x$  arrays and then splined.

Next, since we need to integrate across many spherical Bessel functions, we created splines of these to drastically lower computation times. To do this we implemented a function which computed the argument  $z \equiv k(\eta_0 - \eta(x))$  in the interval  $z \in [0, \eta_0 k_{\text{max}}]$  where  $k_{\text{max}} = 0.3/\text{Mpc}$

as before. Since the spherical Bessel functions oscillate with a period  $2\pi$ , to achieve a sufficiently high sampling resolution we sample with a rate  $\Delta z = 2\pi/n_{\text{bes}}$  where we used  $n_{\text{bes}} = 25$ . This function then runs through all desired values of  $\ell$ , splines each  $j_\ell$  and saves them to an array. The particular  $\ell$  values used in this section are  $\ell \in \{2, 3, 4, 5, 6, 7, 8, 10, 12, 15, 20, 25, 30, 40, 50, 60, 70, 80, 90, 100, 120, 140, 160, 180, 200, 225, 250, 275, 300, \dots, 2000\}$  where  $\dots$  represents intervals of 50.

With the Bessel functions and the source function at hand we are then in a position to perform the LOS integration technique. We began by creating a  $k$  array where  $k \in [k_{\text{min}}, k_{\text{max}}]$  with linear spacing  $\Delta k = 2\pi/(\eta_0 n_k)$  and  $k_{\text{min}}$  is the same as in section 3. We then used this array together with the source function to integrate over the various  $\ell$  values using (42) to obtain  $\Theta_\ell$  where we used the trapezoid integration method and the results were splined. Note that we only integrated in the range  $x \in [-8, 0]$  to save computation times as the source function gives next to no contribution before  $\tilde{g}$ ,  $\Theta_2$  and their derivatives become sufficiently large which happens around recombination. From here it was then a simple task to compute the integral in (44) to solve for  $C_\ell$ ; again using the trapezoid method and finally splined various of the results.

The results were then all written to various data files where we multiplied  $C_\ell$  by  $\frac{\ell(\ell+1)}{2\pi} (10^6 T_{\text{CMB0}})^2$  due to usual conventions. These data files were exported to Python and plotted from there. Additionally, a CMB map was created with the use of the Python library **Healpy** using a set seed to pick a particular set of values from a Gaussian random field which manifests as perturbations in our model of the Universe. Credits to Anton Andreas Brekke for creating this as there were some unfortunate technical difficulties which stopped me from being able to create this myself.

## 4.3. Results

### 4.3.1. Transfer function and integrand

To be able to more easily understand the main results, we plotted the transfer function  $\Theta_\ell$  and part of the integrand in (44) for  $\ell \in \{5, 20, 100, 200, 1000\}$  which are given in Fig. 18 and 19 respectively. The integrand essentially works as an on- and off-switch for the various  $C_\ell$  and can thus tell us when we should expect to see the power increase for the various scales. Note that we plot this in dimensionless units  $k\eta_0$ . So if e.g.  $k\eta_0 = 100$  then we are looking at scales which have the size of order  $\sim 1\%$  of the radius of the observable Universe. This then gives us a mapping between the different  $\ell$  and the scales  $k$ , e.g. we can see  $\ell = 5$  mainly gives its contribution at very large scales, e.g.  $2 \lesssim k\eta_0 \lesssim 10$ . The largest relative peak with this particular normalization is for  $\ell \sim 200$  which is a result that we will probe in more detail later.



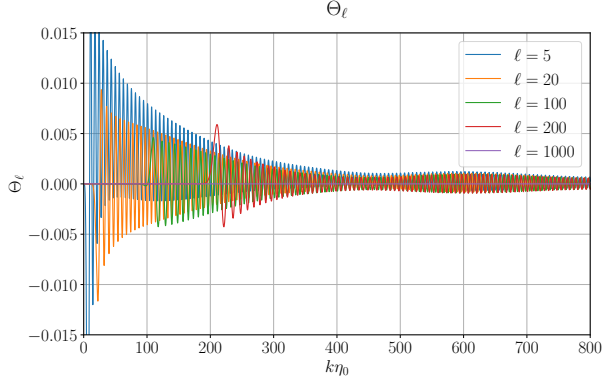


Fig. 18. Transfer function  $\Theta_\ell$  with  $\ell \in \{5, 20, 100, 200, 1000\}$ .

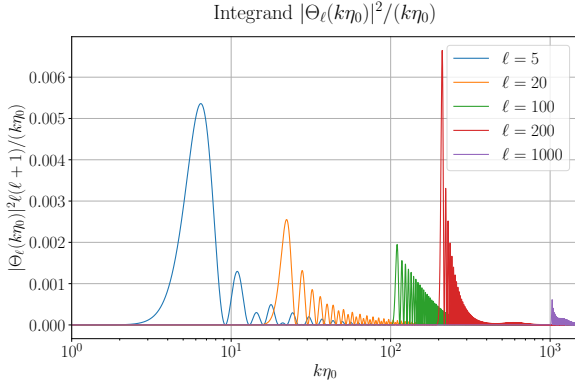


Fig. 19. Integrand  $|\Theta_\ell(k\eta_0)|^2$  with a normalization for each  $\ell \in \{5, 20, 100, 200, 1000\}$  such that they are visible in the plot.

#### 4.3.2. CMB power spectrum

We begin by looking at the CMB power spectrum which is compared to low- and high  $\ell$  data from [2] given in orange and red respectively depicted in Fig. 20. The green shaded region is the cosmic variance which was explained in the theory section. As we can see this variance is quite large for low values  $\ell$  as expected from the previous discussion due to having a small number of possible data points.

The low  $\ell$  values can be seen to be relatively flat compared to the rest of the power spectra. To get a clearer view of the large scale physics Fig. 21 shows a zoomed in view of the CMB spectrum, once again compared to data from [2]. Here we can see the cosmic variance in action, which forces very large error bars in this region. This is not due to “poor” measurements, but instead that the number of data points is simply too small for the data to be statistically accurate. We see that our numerical data is in good agreement with the experimental data, although a relatively large deviation can be seen around  $20 < \ell < 30$ . The error-bars of these data points are however still within the cosmic variance region as can be

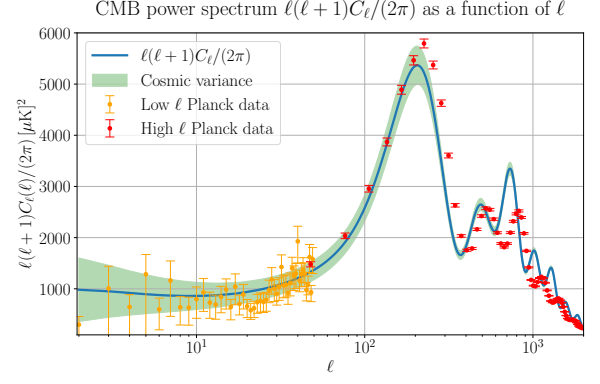


Fig. 20. CMB power spectrum  $C_\ell$  plotted in conventional units and normalization as a function of photon multipole  $\ell$  compared to data from [2].

seen from the previous figure. The exact reasoning other than a potential statistical anomaly is not known, and may be a sign of new physics. The flatness of the power spectra at these scales is to be expected from the initial conditions set up by inflation. At these very large scales, as we have already seen before, there is no causal connection between the disconnected regions post inflation. Thus no changes are to be expected until one reaches scales where the modes may have entered the horizon before recombination occurred. This can be formulated mathematically via the Sachs-Wolfe effect which tells us that we expect to see a flattened curve for small  $\ell$  [4]. This so-called Sachs-Wolfe plateau indicates that there should exist large scale structures in the universe due to its high power at the smallest  $\ell$ 's and can be used to probe the initial conditions stemming from inflation.

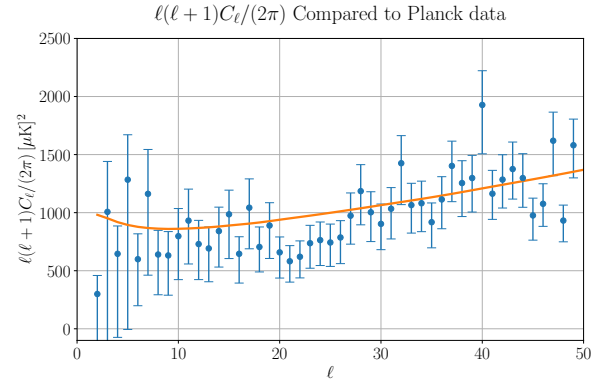


Fig. 21. Low  $\ell$  numerical values for  $C_\ell$  compared to data from [2]

Going down the scales to larger  $\ell$  in Fig. 20 we consider the first 3 peaks. These peaks are the result of the acoustic oscillations from the time before recombination. These oscillations were clearly seen in the previous section where we looked at the matter density perturbations as a function of  $x$ . There are some clear discrepancies in

our numerical results compared to the data. This is an expected result from the fact that we have ignored any heavier elements than Hydrogen together with not accounting for effects from polarization and neutrinos.

The first peak at  $\ell \sim 200$  which corresponds to the first contraction of the primordial plasma. This is the largest scale in which we see one of these compressions occur and corresponds to the scales on the order of the sound horizon at the time of last scattering. The horizontal position of this peak can be used as clear evidence to probe the inherent curvature of the Universe. If we consider that instead our universe was open but that recombination still followed the same inhomogeneities as a flat universe. In this hypothetical universe, photon paths coming towards us would converge from initially starting at larger scales but ending up having a smaller angular distance when they arrive. Thus we would perceive these photons as coming from higher  $\ell$  and all the peaks in the power spectrum would shift to the right. A similar analysis can be made for a closed universe, thus the position of this peak rules out a non flat universe. Note however that there is a large degeneracy in the parameter space. For example changing the number density of baryons would also shift the peak to the right. However the peak would also grow massively in comparison to the shift.

The next two peaks are the result of a decompression and a compression respectively. Modes related to these enter the horizon and earlier times, i.e. during radiation domination. Due to this, their power are relatively low compared to the first peak due to allowing for more causal physics to have brought the plasma to an equilibrium, lowering their respective correlation at these scales. This effect essentially causes hot photons to move towards colder regions and is known as **diffusion damping**. However note that there is a so-called *driving force* which causes the relative size of the third peak to grow. This can be understood by considering a coupled harmonic oscillator; Once the gravitational wells begin to flatten out in certain areas, the surplus of energy will go into increasing the amplitude of the oscillations. This is what causes the third peak to be relatively large compared to the peak before it. Our data is however not entirely in line with the observational data, and is most prominently seen for the third peak. This is due to there being an additional outward drag from the effects of neutrinos, whom we have ignored, which lowers the effect of the driving force during this second compression. Going further down we see that these peaks and troughs continue downwards in an oscillating pattern.

The end of the spectra then corresponds to the diffusion tail, where the diffusion of hot photons quickly become more impactful due to the smaller scales. This then causes the power to quickly diminish as we go to smaller scales. Note that an important use of this data is that the ratio of the power corresponding to compression to decompression can be used as a measurement tool to determine the baryon density today.

Further, mostly for satisfaction, we adjust our CMB

power spectrum in a way which approximates the effects of polarization and neutrinos given in Fig. 22. Note that we do not want to interpret this figure too much as the numerical data has been altered. It is however nice to see that relatively minor alteration is needed to cheat our way to roughly account for neutrinos, heavier elements and polarization.

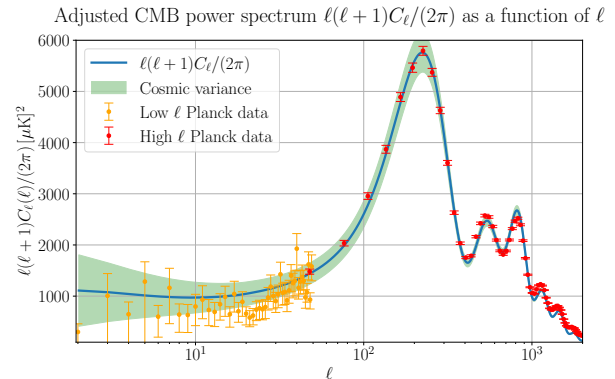


Fig. 22. Adjusted CMB power spectrum where we take  $\ell \rightarrow \ell^{1.018}$  and  $C_\ell \rightarrow 1.13 \cdot C_\ell \exp \left[ -1.25 \cdot 10^{-5} \sqrt{2} \cdot \ell^{3/2} \right]$  compared to data from [2]. Note that this is **completely arbitrary** and only done to approximate the missing shifts of peaks due to effects from helium and neutrino damping.

#### 4.4. Matter power spectrum

We then have the matter power spectrum  $P_M$  given in Fig. 23. Here the vertical dashed line shows the mode which enters the horizon once we have matter-radiation equality. Note that this quantity varies quite significantly as it is a function of  $\mathcal{H}$  which is yet again a function of  $x$  whose particular value we find via searching through a discrete array. As such, we went back to the first part of our code to increase the number of points to get a more accurate reading for this value. The matter power spectrum can be understood as an ensemble of two-point correlation functions which have then been Fourier transformed. Experimentally one would measure the distance between many galaxies and find the amplitude of how often structures seem to form given a particular distance. Then Fourier transforming these two-point correlation functions one arrives at the matter power spectrum. The left and right hand side of the  $k_{eq}$  line can be understood as the scales which entered the horizon after and before radiation-matter equality respectively.

We first consider the right hand side of  $k_{eq}$  as this is where phenomena in the early universe as more prominently shown. During radiation domination the baryons density fluctuations however oscillate together with the photons as we saw in the previous section in Fig. 11. Since the horizon has not had much time to grow at this stage, only the smaller scales perceive some slight oscil-

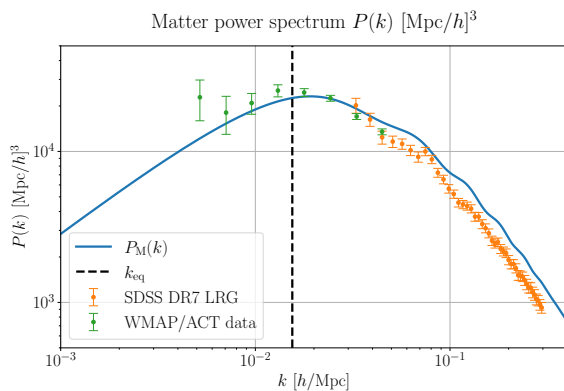


Fig. 23. Matter power spectrum  $P_M$  as a function of Fourier mode  $k$ . The dotted line represents the equality scale, which is the  $k$ -value which corresponds to the mode entering the horizon at time of radiation-matter equality. The green points is data from [10] whilst the orange points are from [11].

lations, which can be seen to only occur on sub-horizon scales when radiation-matter equality occurred. During this time, the CDM density perturbations grow linearly with respect to  $x$  during radiation domination once their respective mode enters the horizon. Since the universe grows at a relatively fast pace during radiation domination these overdensities are thus mostly washed out. This in turn causes the matter power spectrum to be suppressed relative to the larger scales which we can clearly see in the figure.

The left hand side is then the modes are much larger than the horizon at radiation-matter equality. These scales are too large to notice the effect of the acoustic oscillations as their modes are at super-horizon scales by the time the acoustic oscillations stop. Increasing slope that we see on the left hand side is purely due to the initial conditions which were set up by inflation. These scales have no structure formation other than the perturbations from the inflaton field. If one were to have no interactions bar the inflation perturbations matter power spectrum would simply continue to increase with  $P(k) \propto k$ .

The scales  $k \sim k_{\text{eq}}$  are the ones which experience the least amount of suppression. As mentioned, these are the scales whose mode enters the horizon at the time of radiation-matter equality. At this time the expansion of the universe is slower than during radiation domination, yet the scales are small enough to properly build up their overdensities and is thus where the matter power spectrum peaks. This overdensity peak is what is known as the **baryon acoustic oscillation peak** and corresponds to where we expect to see the largest cosmological structure form.

## 4.5. Summary

We used the data from section 3 together with the LOS integration technique to more efficiently be able to calculate a large ensemble of temperature fluctuations  $\Theta_\ell$  using (42). These were then used to calculate the CMB power spectrum  $C_\ell$  with (45). Next we computed the matter power spectrum using (46) and both the power spectra were compared to data and analyzed in detail.

## 5. CMB MAP

At last, with the values of  $C_\ell$  from Fig. 20 we can then create a CMB map given in Fig. 24. As mentioned in the implementations section this figure was generated by one of my co-students Anton Andreas Brekke who also created the corresponding colormap to match the various known CMB maps from actual data.

## 6. CONCLUSION

In this project we solved the unperturbed FLRW background and determined various important epochs. We then took a deep dive into the recombination history of the universe where we determined the time when and at what scales one should expect to see the effects of the CMB photons. Further we perturbed the isotropic and homogeneous universe by using inflation as our model for initial conditions. At last we computed the famous CMB and matter power spectra. The data has a noticeable discrepancy from experimental data due to ignoring the effects of neutrinos, polarization, reionization and heavier elements than Hydrogen, but is overall still a worthwhile endeavour to be able to effectively comprehend the largest scales. Even without including the complications from the ignored effects we are still able to give a qualitative explanation of the underlying physics, explain the two main questions posed in the introduction and accomplish the main goal of creating a Boltzmann-Einstein solver for the CMB power spectrum.

## ACKNOWLEDGMENTS

Many thanks to Hans Arnold Winther for providing detailed feedback on the various milestones together with his great website and programming template which make this project accessible for someone with a relatively poor programming background such as myself. Anton Andreas Brekke has also been a major help regarding talking through the various complicated subjects such that we both could get a better understanding of the underlying physics. This together with helping troubleshooting the various numerical programs needed for this project has been a major help.



# CMB map

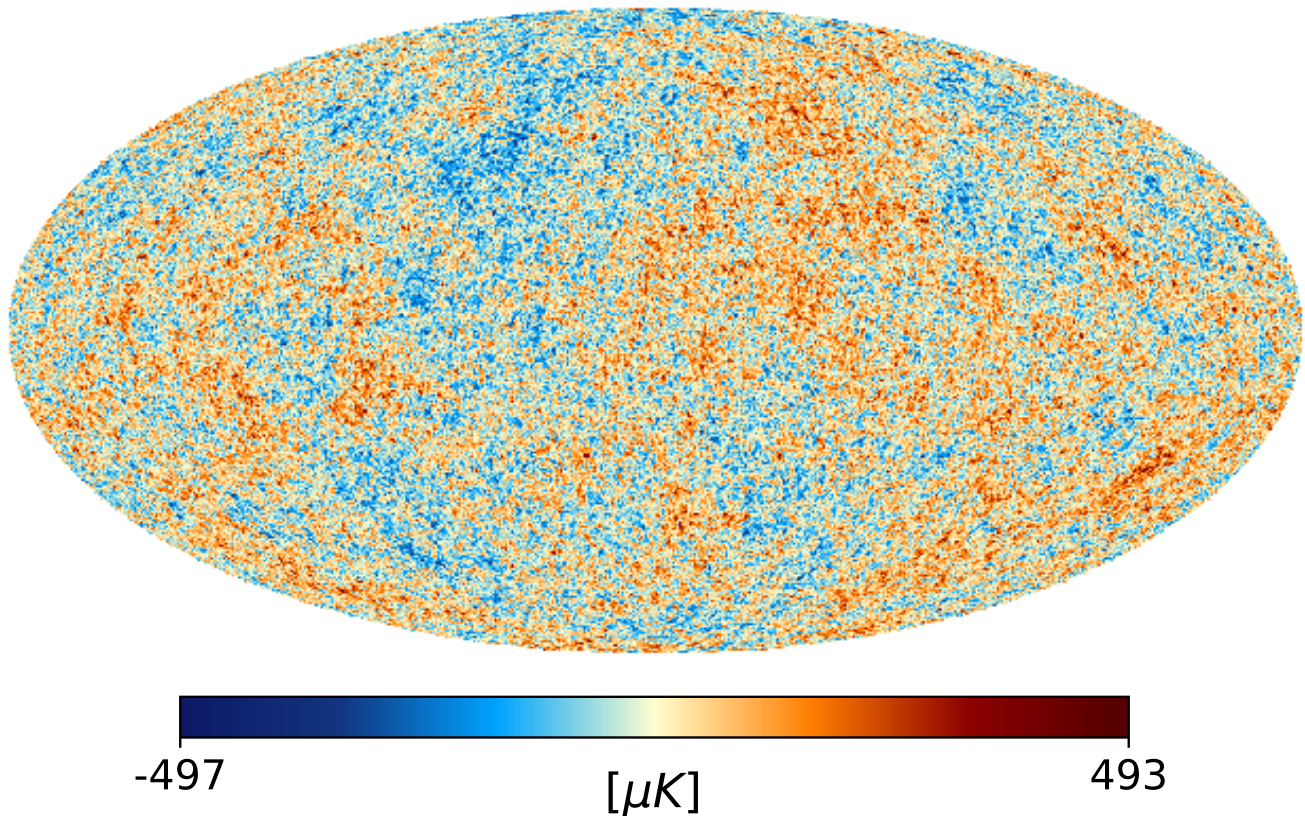


Fig. 24. CMB map. Credits to Anton Andreas Brekke for creating the map and the corresponding cmap. Neither Healpy nor HealPIX would properly install for me, hence I was sadly not able to create this map myself.

- 
- [1] H. A. Winther, H. K. Eriksen, O. Elgaroy, D. F. Mota, and H. Ihle, “Cosmology II.” <https://cmb.wintherscoming.no/>, 2023. Accessed on March 1, 2023.
  - [2] Planck: N. Aghanim *et. al.*, *Planck 2018 results. VI. Cosmological parameters*, *Astron. Astrophys.* **641** (2020) A6, [[arXiv:1807.06209](https://arxiv.org/abs/1807.06209)]. [Erratum: *Astron. Astrophys.* 652, C4 (2021)].
  - [3] SDSS: M. Betoule *et. al.*, *Improved cosmological constraints from a joint analysis of the SDSS-II and SNLS supernova samples*, *Astron. Astrophys.* **568** (2014) A22, [[arXiv:1401.4064](https://arxiv.org/abs/1401.4064)].
  - [4] S. Dodelson, *Modern Cosmology*. Academic Press, Amsterdam, 2003.
  - [5] T. M. Davis and C. H. Lineweaver, *Expanding confusion: Common misconceptions of cosmological horizons and the superluminal expansion of the universe*, *Publications of the Astronomical Society of Australia* **21** (2004) 97–109.
  - [6] J. R. Gott, III, M. Juric, *et. al.*, *A map of the universe*, *Astrophys. J.* **624** (2005) 463, [[astro-ph/0310571](https://arxiv.org/abs/astro-ph/0310571)].
  - [7] E. Di Valentino, O. Mena, *et. al.*, *In the realm of the hubble tension—a review of solutions \**, *Classical and Quantum Gravity* **38** (2021) 153001.
  - [8] S. M. Carroll, *Spacetime and Geometry: An Introduction to General Relativity*. Cambridge University Press, 2019.
  - [9] M. Doran, *Speeding up cosmological Boltzmann codes*, *JCAP* **06** (2005) 011, [[astro-ph/0503277](https://arxiv.org/abs/astro-ph/0503277)].
  - [10] R. Hlozek, J. Dunkley, *et. al.*, *The atacama cosmology telescope: A measurement of the primordial power spectrum*, *The Astrophysical Journal* **749** (2012) 90.
  - [11] B. A. Reid, W. J. Percival, *et. al.*, *Cosmological constraints from the clustering of the sloan digital sky survey dr7 luminous red galaxies*, *Monthly Notices of the Royal Astronomical Society* (2010).